Check for updates

ADVANCED MATERIALS
www.advmat.de

Customized Intranasal Hydrogel Delivering Methylene Blue Ameliorates Cognitive Dysfunction against Alzheimer's Disease

Yujing Liu, Yun Tan, Guopan Cheng, Yaqiong Ni, Aihua Xie, Xiaozhen Zhu, Chao Yin, Yi Zhang, and Tongkai Chen**

The accumulation of hyperphosphorylated tau protein aggregates is a key pathogenic event in Alzheimer's disease (AD) and induces mitochondrial dysfunction and reactive oxygen species overproduction. However, the treatment of AD remains challenging owning to the hindrance caused by the blood–brain barrier (BBB) and the complex pathology of AD. Nasal delivery represents an effective means of circumventing the BBB and delivering drugs to the brain. In this study, black phosphorus (BP) is used as a drug carrier, as well as an antioxidant, and loaded with a tau aggregation inhibitor, methylene blue (MB), to obtain BP-MB. For intranasal (IN) delivery, a thermosensitive hydrogel is fabricated by cross-linking carboxymethyl chitosan and aldehyde Pluronic F127 (F127-CHO) micelles. The BP-MB nanocomposite is incorporated into the hydrogel to obtain BP-MB@Gel. BP-MB@Gel could be injected intranasally, providing high nasal mucosal retention and controlled drug release. After IN administration, BP-MB is continuously released and delivered to the brain, exerting synergistic therapeutic effects by suppressing tau neuropathology, restoring mitochondrial function, and alleviating neuroinflammation, thus inducing cognitive improvements in mouse models of AD. These findings highlight a potential strategy for brain-targeted drug delivery in the management of the complex pathologies of AD.

1. Introduction

Alzheimer's disease (AD) is among the most prevalent neurodegenerative diseases worldwide, affecting an estimated 50 million individuals globally. The disease is characterized by memory loss and cognitive dysfunction, and its burden is continuously increasing with population aging.[1] Extracellular deposits (plaques) of amyloid-β (Aβ) and intracellular neurofibrillary tangles (NFTs) composed of hyperphosphorylated tau (p-tau) aggregates are considered the hallmarks of AD.[2] However, over the past few decades, most AD clinical trials targeting the Aβ burden have largely been unsuccessful. Therefore, more attention has been paid to tau-targeting therapies, particularly because tau pathology appears to be more closely linked to cognitive decline than Aβ accumulation.[3]

Tau is a microtubule (MT)-associated protein that is mainly expressed in neurons, contributing to the stability of axonal MTs and regulating axonal transport and growth.[4] In AD, tau shows elevated levels of phosphorylation, which causes it to detach from microtubules and undergo oligomerization and self-aggregation to generate NFTs.[5] The pathophysiology of tau includes the disruption of the axonal transport of organelles, such as mitochondria, which ultimately leads to synaptic dysfunction.[6] Mitochondrial are fundamental subcellular organelles and play an essential role in providing bio-energy to neurons. Notably, previous studies indicate that hyperphosphorylated tau impairs mitochondrial function by enhancing mitochondrial fission and impairing mitochondrial transport, thus decreasing adenosine triphosphate (ATP) production and increasing oxidative stress.[7] In turn, mitochondrial oxidative stress promotes the abnormal phosphorylation and polymerization of tau by inducing an imbalance of protein phosphatases and kinases.[8] This results in a vicious circle and promotes AD progression. Therefore, mitigating oxidative stress, restoring mitochondrial function, and inhibiting p-tau aggregation simultaneously could be a promising strategy for AD treatment.[9]

One strategy to directly target tau involves blocking its aggregation. Methylene blue (MB), a widely studied drug that has been proven to prevent tau aggregation and attenuate tau phosphorylation, shows beneficial effects on AD and memory improvement.[10] However, the short systemic half-life and

Y. Liu, G. Cheng, A. Xie, X. Zhu, T. Chen
Science and Technology Innovation Center
Guangzhou University of Chinese Medicine
Guangzhou 510405, China
E-mail: chentongkai@gzucm.edu.cn
Y. Tan, Y. Ni, C. Yin, Y. Zhang
Hunan Provincial Key Laboratory of Micro & Nano Materials Interface Science
College of Chemistry and Chemical Engineering
Central South University
Changsha 410083, China
E-mail: yzhangcsu@csu.edu.cn
The ORCID identification number(s) for the author(s) of this article can be found under https://doi.org/10.1002/adma.202307081

DOI: 10.1002/adma.202307081

 © 2024 Wiley-VCH GmbH

insufficient brain accumulation of MB limit its efficacy in AD therapy. Therefore, additional drug delivery methods should be explored to improve the targeted delivery efficiency and bioavailability of MB.

Nanocarriers have been widely applied as drug delivery agents to improve drug biodistribution and enhance their targeting. Among them, black phosphorus nanosheets (BP NSs) are a novel type of 2D nanomaterial consisting of puckered honeycomb layers of phosphorus (P) atoms that are connected via strong intralayer P—P bonds and weak inter-layer van der Waals forces.[11] Due to their benign elemental composition (P), large surface area, photosensitivity, broad light absorption spectrum, and natural biodegradability,[12] BP NSs have attracted immense interest in biomedical applications including neurodegenerative disease therapy. The negative charge and corrugated surface structure of BP NSs make them ideal vehicles for drug loading. Moreover, their photothermal effect has been demonstrated to increase the permeability of the blood–brain barrier (BBB) to allow brain-targeted drug delivery. In our previous reports, BP NSs-based drug delivery nanoplatforms were constructed to treat Parkinson's disease and achieved a satisfactory outcome, alleviating the associated symptoms.[13] In another study, BP NSs were confirmed to have chemically reacted with reactive oxygen species (ROS) and finally degraded into non-toxic phosphorus oxides,[14] indicating their great potential in managing oxidative stress-related diseases management. Given these characteristics, BP NSs could not only act as drug carriers for MB but also function as nanocaptors to scavenge excessive ROS. However, the antioxidant capacity of BP NSs has not been investigated in AD treatment.

Another challenge in AD treatment is the BBB, which is formed by the monolayer of tightly-sealed endothelial cells along the vascular tree. These cells have low paracellular and transcellular permeability[15] and thus restrict the passage of therapeutic drugs from the blood to the brain parenchyma. Intranasal (IN) administration has emerged as a promising and feasible alternative that circumvents the BBB and directly introduces therapeutics to the brain via the olfactory and trigeminal nerves.[16] Unlike oral delivery, systemic administration, and intracerebroventricular injection, the IN route avoids first-pass metabolism, gastrointestinal exposure, systemic clearance, and the hindrance caused by the BBB, making it a patient-friendly and effective treatment option for neurological disorders. The highly vascularized nasal mucosa serves as the main site for drug absorption and deposition.[17] However, nasal drug delivery also presents several obstacles, including mucociliary clearance, the low permeability of the nasal epithelium, enzymatic degradation, and a short drug retention time, substantially curtailing the efficacy of IN therapy.[18] Therefore, a suitable mucoadhesive system is necessary to resolve these limitations.[19] A desirable candidate for such a system is hydrogels, which are characterized by water-rich (above 90 wt%) 3D cross-linked polymer networks.[20] In particular, injectable thermoresponsive hydrogels are promising IN delivery vehicles, as they can be easily administrated in their initial liquid state and transformed into a gel in response to thermal stimuli.[21] These viscous hydrogels can adhere to the nasal mucosa, serving as a depot for sustained drug release, thus facilitating drug absorption through the nasal epithelium. Due to their porous network structure, hydrogels can also be loaded with various therapeutic agents.[22]

Modification via dynamic covalent bonds or physical bonds is an effective strategy for improving the physicochemical properties of a hydrogel.[23] As shown in **Figure 1**, in this study, a hydrogel system was constructed via a Schiff-based reaction between carboxymethyl chitosan (CMCS) and aldehyde Pluronic F127 (F127-CHO, FC) micelles. MB was loaded onto BP NSs to yield BP-MB nanocomposites, which were then incorporated into the fabricated F127-CHO/CMCS (F/C) hydrogel. F127-CHO, an amphiphilic triblock copolymer with temperature-responsive gelation capacity, provided aldehyde groups that reacted with the amine groups of CMCS to form dynamic and reversible Schiff-base linkages, making the hydrogel injectable and giving it self-healing capacity. Our in vitro study showed that BP-MB nanocomposites could scavenge multiple types of ROS and protect neurons form okadaic acid (OA)-induced damage by reducing oxidative stress, improving mitochondrial function, and inhibiting tau protein aggregation. To expand these results in an in vivo context, we used the F/C hydrogel platform for the nasal delivery of BP-MB (BP-MB@Gel). The resultant BP-MB@Gel was able to bypass the BBB and increase drug accumulation in the brain, ultimately reversing cognitive deficits, reducing neuronal injury, and restoring brain glucose metabolism in OA-induced AD models. Further examination indicated that the therapeutic effects of BP-MB@Gel were mediated by the inhibition of tau phosphorylation, mitochondrial protection, antioxidative effects, and the alleviation of neuroinflammation. Collectively, the results show that the BP-MB@Gel can serve as a useful tool for brain-targeted AD therapy.

2. Results and Discussion

2.1. Characteristics of BP NSs and BP-MB

BP NSs were prepared using a classic liquid-phase exfoliation method as described previously.[13] Transmission electron microscopy (TEM) and scanning electron microscopy (SEM) demonstrated that the synthesized BP NSs had a typical 2D flake morphology with a size of about 200 nm (**Figures 2A** and S1, Supporting Information). In addition, elemental mapping indicated the distribution of P and O were within the BP NSs (Figure S1, Supporting Information). Atomic force microscopy (AFM) images further confirmed the thin layer structure of the BP NSs (thickness: 6 nm) (Figure S2, Supporting Information). Dynamic light scattering (DLS) experiments showed that the hydrodynamic size and zeta potential of BP NSs were 187.9 nm and −33.76 mV, respectively (Figure 2B,D). Further, the UV–vis absorbance spectrum of the BP NSs (Figure 2C) was consistent with the reported literature.[24] These results validated the successful preparation of BP NSs.

According to previous reports, cationic MB can be absorbed into BP NSs via electrostatic interaction according to previous reports.[25] The BP-MB synthesized in this study retained a 2D morphology, as visualized via TEM (Figure 2E). Meanwhile, compared to bare BP NSs, BP-MB showed a remarkable increase in hydrodynamic size (291 nm) and zeta potential (−26.34 mV), as well as noticeable color changes, further verifying the successful loading of MB (Figure 2F and Figure S3, Supporting

© 2024 Wiley-VCH GmbH

Downloaded for personal academic use. All rights reserved. https://papernode.online/

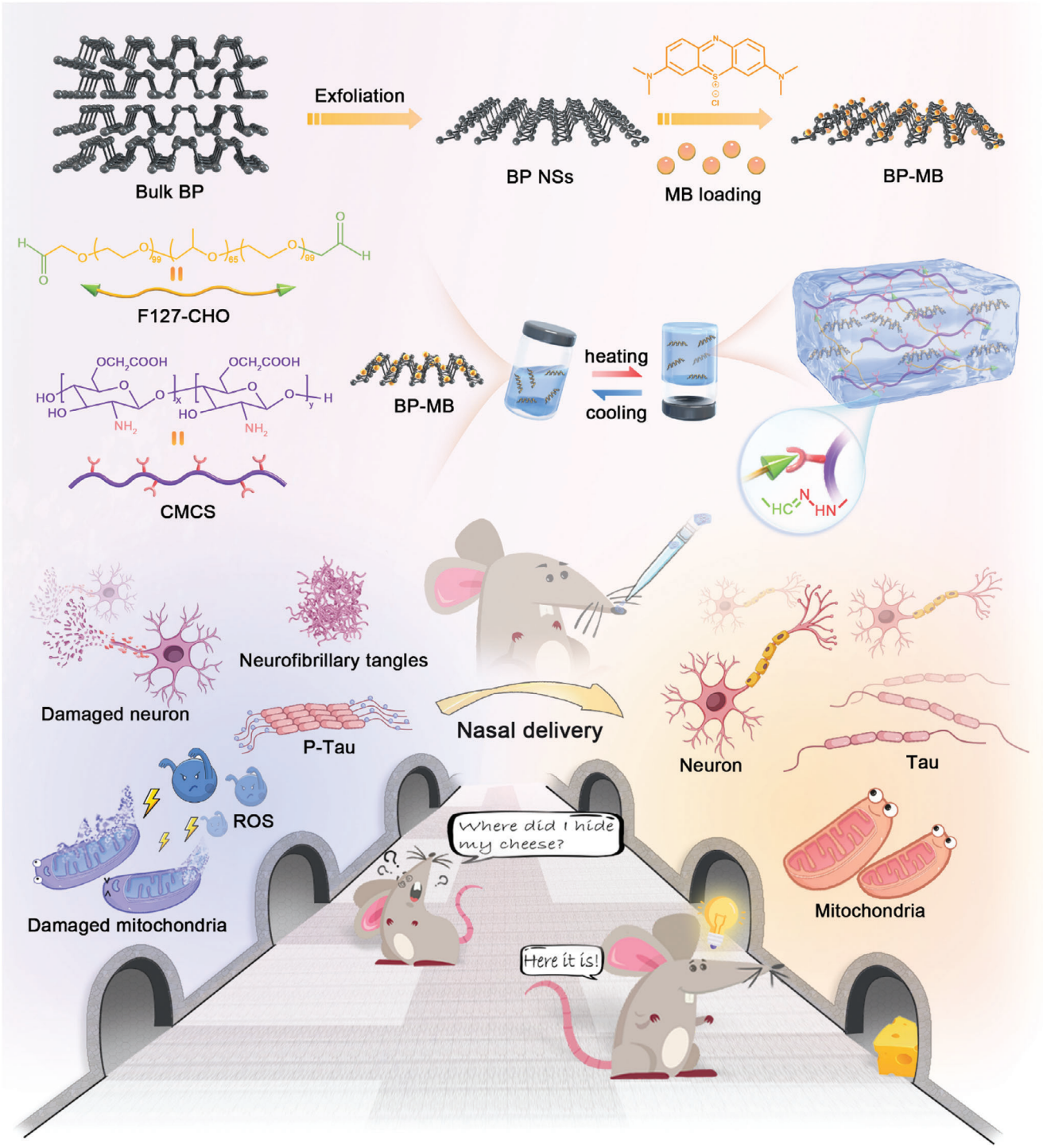

Figure 1. Schematic overview of the preparation of BP-MB@Gel and its application for improving AD pathology.

Information). The drug loading capacity was determined using UV–vis spectroscopy. As shown in Figure 2G, BP-MB showed characteristic absorption peaks at 292 and 664 nm, indicating the interaction between BP and MB. Furthermore, the loading capacity increased in a feeding amount-dependent manner (Figure 2H). SEM image and elemental mapping in Figure 2I further demonstrated that the elements P, C, S, and N elements all coexisted in BP-MB. AFM analysis found that the thickness of the nanosheets after MB absorption decreased slightly from 6 to 4 nm (Figure 2J,K), consistent with a previous study.[25a]

ROS overproduction is a typical characteristic of oxidative stress and a significant initiator of neuronal damage and thus

© 2024 Wiley-VCH GmbH

Downloaded for personal academic use. All rights reserved. https://papernode.online/

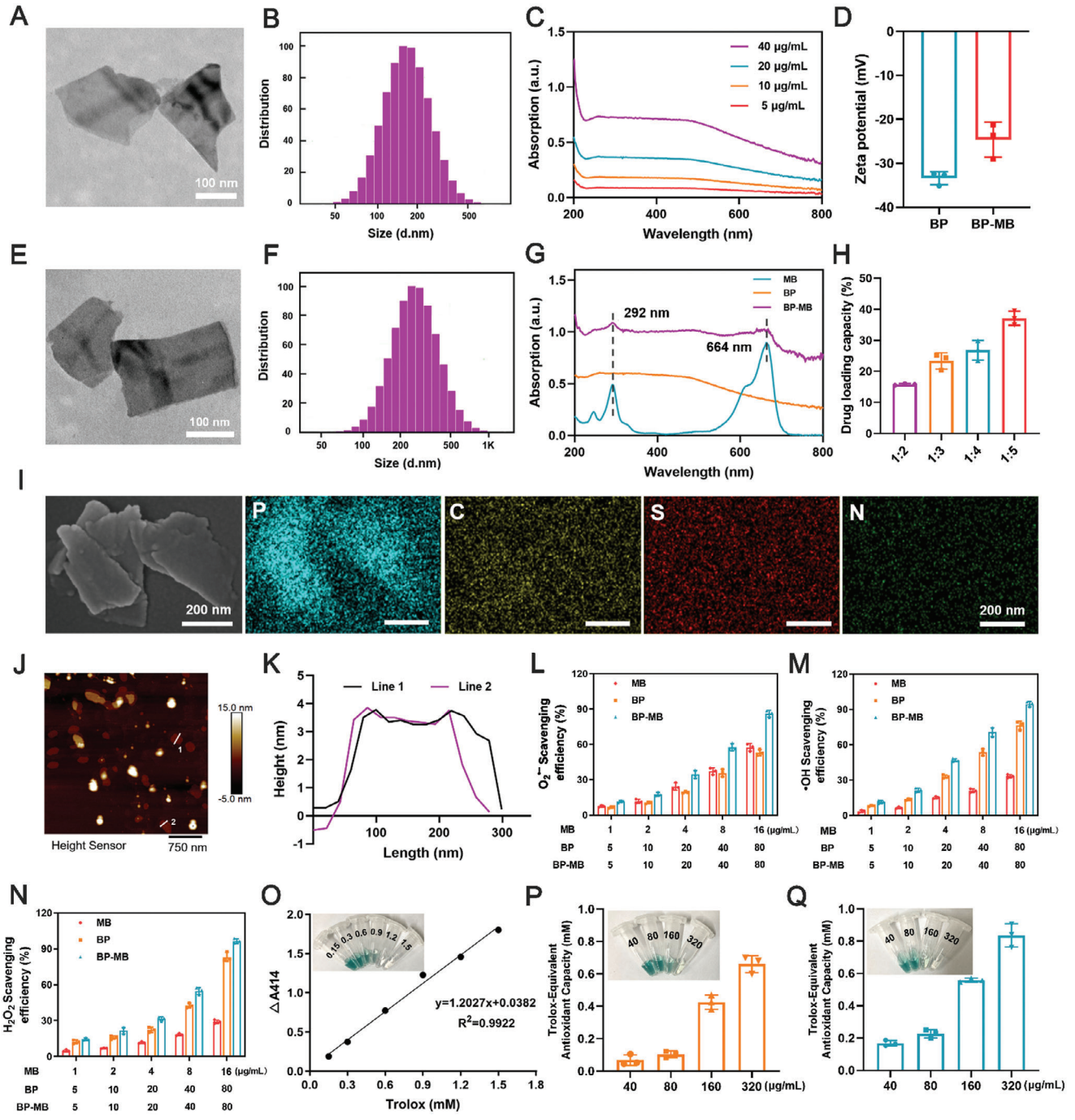

Figure 2. Characteristics of BP NSs and BP-MB. A) Representative TEM image, B) particle size distribution, and C) UV–vis spectrum of a series of concentrations of BP NSs. D) Zeta potential of BP NSs and BP-MB ($n = 3$). E) TEM image of BP-MB. F) Size distribution of BP-MB. G) UV–vis absorption spectra of MB, BP, and BP-MB. H) Drug loading capacity of BP at various feeding ratios of BP: MB (w/w) ($n = 3$). I) SEM image and elemental mapping of BP-MB. J) Typical AFM image and K) height profile curve of BP-MB. L) $O_2^{\bullet-}$, M) ·OH, and N) H_2O_2 scavenging ability of BP NSs ($n = 3$). O) Standard curve and images of Trolox at different concentrations incubated with an ABTS solution. Concentration-dependent antioxidant activity and corresponding photographs of P) BP NSs and Q) BP-MB (with a concentration of 40, 80, 160, and 320 μg mL^{-1}) characterized using the ABTS method ($n = 3$). Data in (D), (H), (L–N), and (P,Q) were processed using GraphPad Prism 8.0 and are presented as the mean ± SD.

© 2024 Wiley-VCH GmbH

Downloaded for personal academic use. All rights reserved. https://papernode.online/

contributes to the pathogenesis and progression of AD. Hence, depleting excessive ROS is a potential strategy for treating the condition.[26] We herein evaluated the antioxidant capacity of MB, BP, and BP-MB against multiple ROS species including $O_2^{\bullet-}$, ·OH, and H_2O_2. As shown in Figure 2L–N, MB, BP, and BP-MB all displayed a concentration-dependent ROS scavenging activity. In addition, at 80 μg mL^{-1}, BP-MB could achieve more than 90% clearance for all ROS. The total antioxidant capacity (T-AOC) was further tested using the T-AOC assay kit. In this assay, ABTS acted as a chromogenic substrate and was oxidized by H_2O_2 to green $ABTS^{\bullet+}$ under the catalysis influence of the peroxidase mimetics. However, antioxidants can inhibit $ABTS^{\bullet+}$ production.[27] The reaction is as follows: $ABTS^{\cdot+} \xrightarrow{\text{Antioxidant}} ABTS$. In this study, Trolox was used as a standard antioxidant reagent to generate a standard curve (Figure 2O). The T-AOC of BP NSs and BP-MB were examined spectrophotometrically and calculated using the Trolox standard curve. As illustrated in Figure 2P,Q, a gradient of green color dodge was clearly observed in the presence of increasing concentrations of BP NSs and BP-MB. Moreover, BP-MB exhibited stronger antioxidative capacity. Therefore, BP-MB could be utilized as an efficient antioxidant for in vivo applications.

2.2. Characterization of BP-MB@Gel

Figure 3A,B illustrates the preparation of cross-linked BP-MB@Gel via a Schiff base reaction between F127-CHO and CMCS. ^{1}H nuclear magnetic resonance (^{1}H NMR) spectroscopy was performed. The formation of covalent bonds in F/C hydrogels was proven by the ^{1}H NMR spectra. As shown in Figure 3C, specifically, compared to the ^{1}H NMR spectrum of F127, the F127-CHO showed a fresh peak at 9.58 ppm in the spectrum, corresponding to the aldehyde (—CHO) group. This indicated that the primary alcohol groups of F127 were oxidized to aldehyde groups. It is worth noting that the peaks corresponding to the Schiff base hydrogen (—CH═N—) appeared at 7–8.5 ppm in the ^{1}H NMR spectrum of the F/C hydrogel, but not in the ^{1}H NMR spectrum of F127-CHO and CMCS. In addition, the peak corresponding to the hydrogen of —CHO disappeared in the ^{1}H NMR spectrum of the F/C hydrogel. This confirmed that the covalent crosslinks in the hydrogel were formed by a Schiff base reaction between F127-CHO and CMCS. The chemical structures of F127-CHO, CMCS, and the F/C hydrogel were further identified using Fourier-transform infrared spectroscopy (FTIR). The characteristic peak at 2888 cm^{-1} was assigned to —CH stretching. Compared with F127, the spectrum of F127-CHO displayed a new absorption peak at 1727 cm^{-1}, which could be attributed to the C═O stretching in the aldehyde group, confirming the successful grafting of an aldehyde group onto the F127 chain. The characteristic peaks at 1583 and 1417 cm^{-1} showed in the FTIR spectrum of CMCS could be attributed to the antisymmetric stretching vibrations and stretching vibration of the $—COO^-$ group, respectively.[28] Thus, the experiments showed that carboxymethyl groups were successfully introduced into the chitosan polymeric chain. Moreover, the absence of the band at 1727 cm^{-1} and the new peak at 1590 cm^{-1} (—C═N) in the F/C hydrogel spectrum proved the occurrence of the Schiff base reaction between the aldehyde groups and the amino groups (Figure 3D).

The properties of a blank hydrogel can be modulated by tuning the concentration ratio of F127-CHO and CMCS. Herein, different concentration ratios of F127-CHO to CMCS including 3:4, 4:4, and 4:5 were chosen for properties optimization investigating. As depicted in Figure S4, Supporting Information, as the temperature increases, the storage modulus (G') gradually exceeds the loss modulus (G''). The temperature at which G'' was equal to G' represented the lower critical solution temperature (LCST). Higher concentrations of CMCS resulted in lower gelation temperatures, and the LCST of these hydrogels was determined to be 29.8, 28.8, and <25 °C, respectively.

The rheological properties of these hydrogels were also studied. G' represents elastic properties, while G'' represents viscous properties. The frequency sweep profiles are displayed in Figure S5, Supporting Information. Under an increasing angular frequency, the G' of these hydrogels with different compositions became apparently higher than their G'', demonstrating the dominant elastic properties of these hydrogels. Moreover, given that the network of the hydrogel can collapse under a certain strain and thus cause a switch from the gel to a quasi-liquid state (when $G'' > G'$), dynamic strain sweep tests were performed. The intersection points between G' and G'' were identified at a strain of 225%, 190%, and 250%, respectively, at ratios of 3:4, 4:4, and 4:5. Hence, these hydrogels would liquefy under a strain beyond these respective thresholds (Figure S6, Supporting Information). Hydrogels with injectable properties allow easy operation during nasal administration. The viscosity of the prepared hydrogels decreased dramatically as the shear rate changed from 0.1 to 100 s^{-1}. This typical shear-thinning behavior reflected the facile injectability of these hydrogels (Figure S7A, Supporting Information).

The blank hydrogel prepared using a concentration ratio of 3:4 exhibited the most optimal LCST (29.8 °C) for in situ gelation upon in vivo application and also showed a large deformation tolerance (with a critical strain of 225%). Hence, we synthesized the F/C hydrogel using this ratio and then loaded BP-MB for further experiments. The incorporation of BP-MB into the F/C hydrogels was confirmed based on the FTIR spectrum. As shown in Figure 3E, the peaks at 1641 and 1001 cm^{-1} in the spectrum of BP corresponded to phosphate groups. For BP-MB, the peak at 1440 cm^{-1} could be assigned to the —C—H bond. Moreover, a broad absorption peak at 3419 cm^{-1} suggested the existence of intermolecular hydrogen bonds in BP-MB. Furthermore, the typical peaks of BP-MB were also detected in the spectrum of BP-MB@Gel, indicating the successful integration of BP-MB into F/C hydrogel. The normal temperature range of the nasal mucosa is about 34 °C.[29] Thermo-sensitive gelation behavior was tested using a vial tilting method, and both the F/C hydrogel and BP-MB@Gel displayed sol–gel transition at 34 °C (Figure 3F). Therefore, the thermosensitive hydrogel remained in the gel state in the nasal mucosa. The morphology of lyophilized hydrogels was examined via SEM and both hydrogels presented a typical interconnected and porous network structure (Figure 3I). Notably, the encapsulation of BP-MB did not change the internal structure of the hydrogel. Compared with the blank gel, BP-MB@Gel showed a higher LCST (31.8 °C), which remained to be a suitable temperature for in situ gelation (Figure 3G). Oscillatory frequency sweep measurements indicated that as the angular frequency

© 2024 Wiley-VCH GmbH

Downloaded for personal academic use. All rights reserved. https://papernode.online/

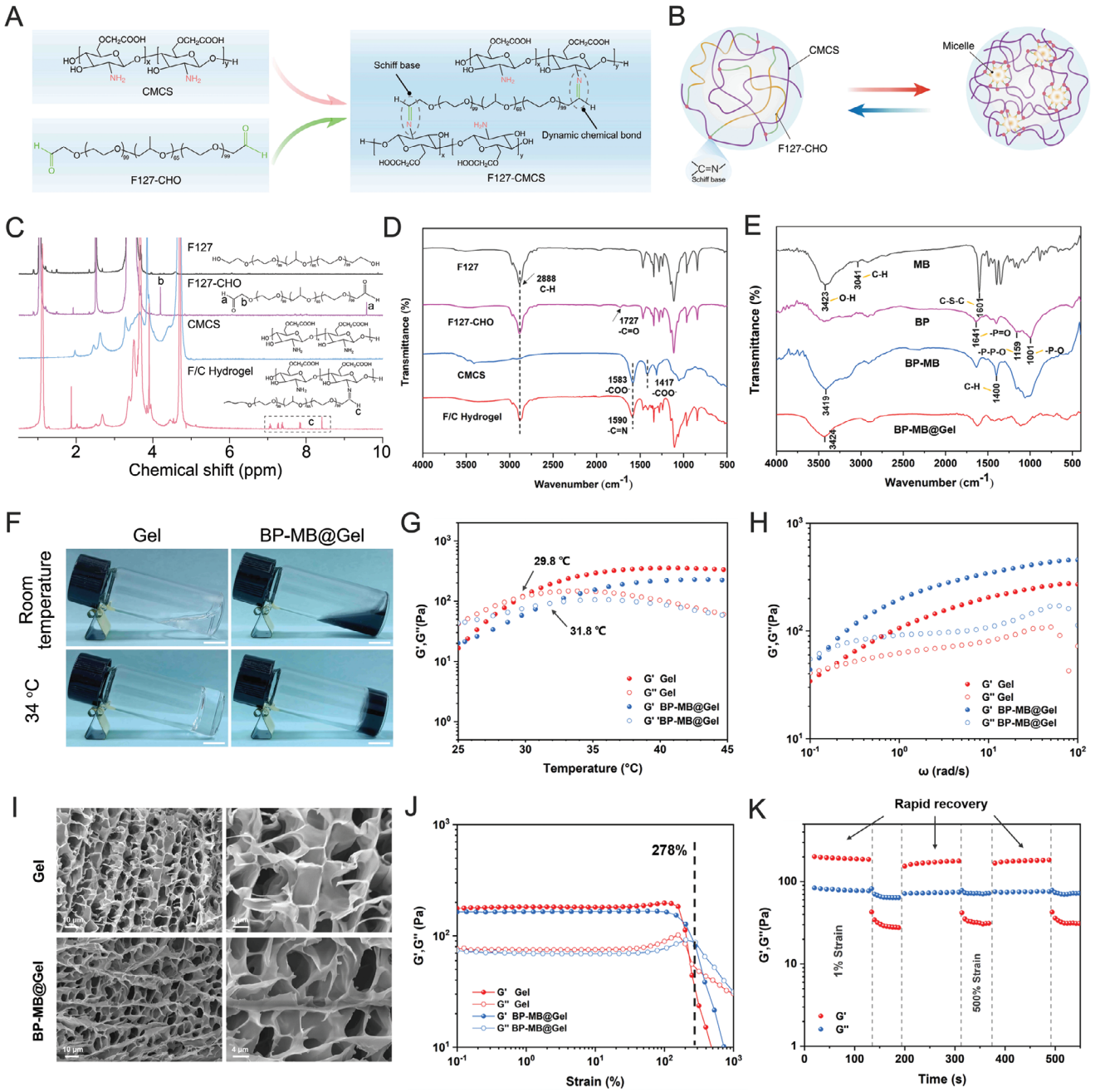

Figure 3. Characterizations of BP-MB@Gel. A) Schematic illustration showing the synthesis process of the F127-CHO/CMCS hydrogel. B) Schematic illustration of the cross-linked F127-CHO/CMCS hydrogel. C) The ^{1}H NMR spectra of F127, F127-CHO, CMCS, and F/C hydrogel. D) FTIR spectra of F127, F127-CHO, CMCS, and the F/C hydrogel synthesized through the Schiff base reaction between F127-CHO and CMCS. E) FTIR spectra of MB, BP, BP-MB, and BP-MB@Gel. F) The optical images of the sol–gel transition of hydrogel in response to changes in temperature. Scale bars: 1 cm. G) Temperature sweep tests and H) frequency sweeps of the blank hydrogels and BP-MB@Gel. I) Representative SEM images (scale bar: 10 μm) and the magnified images (right, scale bar: 4 μm) of the blank hydrogel and BP-MB@Gel. J) Strain sweep of the blank hydrogel and BP-MB@Gel. K) Storage (G') and loss (G'') modulus of BP-MB@Gel at recycled strains.

increased, BP-MB@Gel with an elastic solid state was generated (Figure 3H). In addition, compared with the blank gel, the viscosity of BP-MB@Gel sharply decreased with an increasing shear rate (Figure S7B, Supporting Information), indicating its shear thinning property. This behavior could also be visually verified via an easy injection through a narrow needle (as shown in Video S1, Supporting Information). The strain sweep test demonstrated that BP-MB@Gel would transform from a solid to a fluid state at a strain above 278% (Figure 3J). This threshold was slightly higher than that for the blank hydrogel (225%). Afterward, high-strain and low-strain cyclic scanning tests were conducted to assess the self-healing ability of BP-MB@Gel. Benefiting from the

© 2024 Wiley-VCH GmbH

Downloaded for personal academic use. All rights reserved. https://papernode.online/

reversibility of the dynamic Schiff-base linkages, both G' and G'' dropped sharply at a high strain (500%) but returned quickly to their initial values when the strain reverted to 1%. Notably, this process was repeatable (Figure 3K), illustrating the excellent self-healing properties of BP-MB@Gel.

In order to evaluate the nasal diffusion performance of BP-MB and BP-MB@Gel, in vitro nasal mucosa permeation assays were conducted. The results showed that the initial burst release occurred in the first 12 h, followed by a steady release. Notably, ≈100% of MB was released from BP-MB (97.18%) and BP-MB@Gel (92.81%) within 48 h. Compared to BP-MB, MB-BP@Gel displayed a slower release behavior, suggesting that the hydrogel system prolonged the overall duration of drug release (Figure S8, Supporting Information).

2.3. Transport across the Nasal Mucosal Barrier

To enable the nasal delivery of drugs to the brain, the nasal mucosal barrier needs to be crossed. Therefore, human nasal epithelial cells (HNEpC) were selected as the cellular model to study transport. We first examined the cytotoxicity of different formulations in HNEpC. The CCK-8 assay showed that both BP and BP-MB had good biocompatibility at concentrations of 2.5–40 μg mL^{-1}, while MB exerted obvious cytotoxicity at a concentration of 20 μg mL^{-1} (Figure S9, Supporting Information). We thus chose a suitable concentration of MB (8 μg mL^{-1}) and BP-MB (BP: 40 μg mL^{-1}; MB equivalent: 8 μg mL^{-1}) for subsequent experiments. The transport of drugs through the nasal membrane and the mechanisms underlying this process were explored using a transwell culture model (**Figure** 4A). Free MB displayed a high permeability exceeding 70%, and BP-MB showed comparable permeability (67.43%), indicating that both were effective in crossing the HNEpC monolayer (Figure 4B). Moreover, the transepithelial electrical resistance (TEER) value did not change significantly in treated groups during transport studies (Figure 4C), suggesting that the transcellular movement of MB and BP-MB was due to the transcytosis process from the apical to the basolateral cell membrane rather than due to paracytosis.[30]

We further investigated the transport mechanisms of BP-MB by blocking different transport pathways. To this end, different pharmacological inhibitors were used, as described in Table S1, Supporting Information. The cell viability assay showed that these various inhibitors did not influence the survival of HNEpC (Figure S10, Supporting Information). Monensin and brefeldin A are common inhibitors of the Golgi transport network. Monensin can inhibit the transport from the Golgi apparatus to the plasma membrane (PM), and brefeldin A can block transport from the ER to the Golgi apparatus.[31] Bafilomycin A1 is a V-ATPase inhibitor commonly used to inhibit the reacidification of vesicles after endocytosis.[32] As shown in Figure 4D, the transcellular movement of almost 31% and 40% of BP-MB was blocked in the presence of monensin and brefeldin A, respectively (compared with the control group). Further, bafilomycin A1 treatment had no significant inhibition effects on the transcytosis, suggesting that BP-MB transport mainly involved the ER/Golgi apparatus pathway and Golgi/PM pathways but was largely unrelated to the reacidification of vesicles.

2.4. Endocytosis Mechanisms and Intracellular Trafficking in Human Nasal Epithelial Cells and SH-SY5Y Cells

A detailed understanding of nanocarrier cellular uptake mechanisms is crucial for understanding the biological processing of nanocarriers and the mode of drug action. Herein, Cy5-labeled BP NSs were used for the endocytosis mechanism and intracellular trafficking study. Positively-charged Cy5-PEG-NH_2 was loaded on the negative-charged BP NSs through electrostatic adsorption. As shown in Figures S11 and S12, Supporting Information, the intracellular fluorescence intensity of BP-Cy5 in both HNEpC and SH-SY5Y cells obviously increased with increasing BP-Cy5 concentrations and prolonged incubation durations, indicating that endocytosis was time- and concentration-dependent. Subsequently, we explored the endocytosis pathways for BP-Cy5 using various relevant inhibitors (Table S2, Supporting Information). To ensure the safety and effectiveness of these inhibitors, their appropriate concentrations were determined based on the cytotoxicity results (Figures S13 and S14, Supporting Information). We selected 8 mM of methyl-β-cyclodextrin (MβCD), 0.3 M of hypertonic sucrose (HS), 30 μM of chlorpromazine (CPZ), and 50 μM of 5-(N-Ethyl-N-isopropyl) amiloride (EIPA) for the endocytosis studies in HNEpC cells. Meanwhile, in SH-SY5Y cells, the safe effective concentrations chosen for MβCD, HS, CPZ, and EIPA were 1 mM, 0.2 M, 30 μM, and 50 μM, respectively. Cells incubated with BP-Cy5 without any inhibitors were designated as the control group, and the fluorescence intensity of each group was measured.

The cellular uptake of BP-Cy5 by HNEpC cells is shown in Figure 4G. All the inhibitors apparently reduced the cellular fluorescence intensity of BP-Cy5, indicating that more than one endocytic pathway was involved in the internalization process of BP-Cy5. More specifically, internalization was reduced by 31.3%, 64.5%, 52.1%, and 78.9% in the presence of MβCD, HS, CPZ, and EIPA, respectively (Figure 4K). This indicated that macropinocytosis was predominantly responsible for the endocytosis of BP-Cy5, followed by clathrin-mediated endocytosis. Meanwhile, caveolar-mediated endocytosis played a relatively limited role.

We then extended our analysis to the intracellular trafficking of both free Cy5 and BP-Cy5 following uptake. The colocalization of Cy5 and BP-Cy5 with different subcellular organelles was examined using confocal laser scanning microscopy (CLSM). Three organelles, including lysosomes (Lyso), endoplasmic reticulum (ER), and mitochondria (Mito), were stained using specific trackers, and the degree of colocalization between organelles and both free Cy5 and BP-Cy5 was determined based on Pearson's correlation coefficient (PCC). The colocalization of these markers in HNEpC cells is illustrated in Figure 4H. Here, the regions of yellow fluorescence represent regions of colocalization. The findings suggested that both free Cy5 and BP-Cy5 could be distributed to all these organelles after internalization. Cy5 showed the highest colocalizations with the ER (PCC = 0.69), followed by Lyso (PCC = 0.37) and Mito (PCC = 0.36). However, there were no significant differences in the PCC of BP-Cy5 with the Lyso, ER, and Mito apparatus (0.4, 0.34, and 0.38, respectively) (Figure 4M).

According to the above results, the transmembrane behavior of BP-Cy5 is summarized in Figure 4E. First, BP-Cy5 was mainly taken up through macropinocytosis, but clathrin-and

© 2024 Wiley-VCH GmbH

Downloaded for personal academic use. All rights reserved. https://papernode.online/

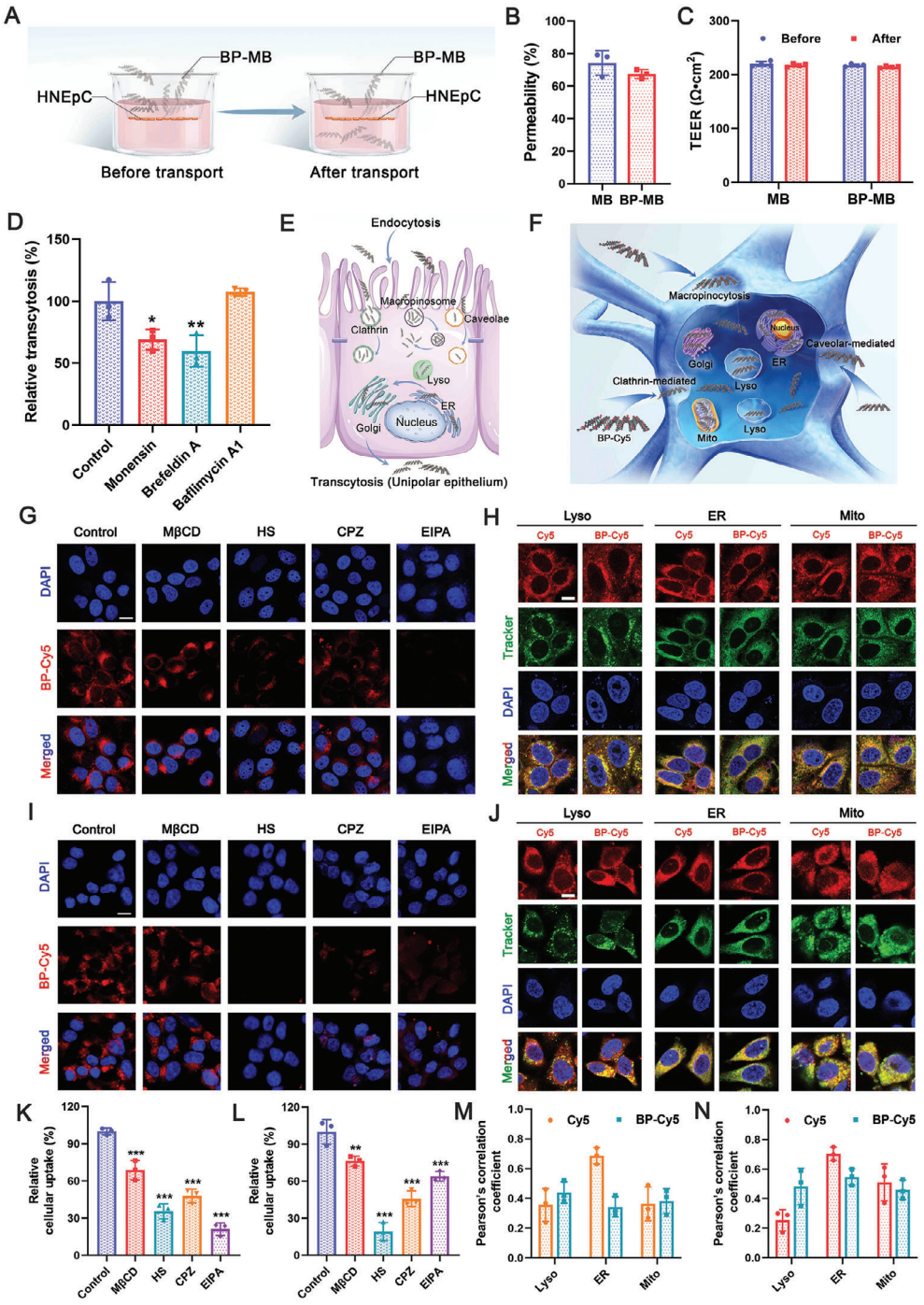

Figure 4. Transportation study of BP-Cy5 across the in vitro nasal mucosal barrier/endocytosis and colocalization of BP-Cy5 in SH-SY5Y cells. A) Schematic illustration of BP-MB transportation across the HNEpC monolayer in the transwell model. B) In vitro nasal mucosal barrier crossing ability of MB and BP-MB ($n = 3$). C) TEER values of HNEpC monolayers before and after the experiment ($n = 3$). D) Transcytosis mechanism investigation of BP-MB through the HNEpC monolayer ($n = 3$). Groups that were not treated with inhibitors were set as the control and their values were normalized to 100%. *$p < 0.05$ and **$p < 0.01$ versus the control group. E) Schematic diagram showing the endocytosis and transmembrane pathways of BP-Cy5 in HNEpC. F) Schematic diagram showing the cellular uptake and transport of BP-Cy5 in SH-SY5Y cells. G) CLSM images showing the effects of various inhibitors on the endocytosis of BP-Cy5 in HNEpC. Scale bar: 50 µm. H) Colocalization of Cy5 and BP-Cy5 with the ER, Lyso, and Mito in HNEpC cells visualized using CLSM. Scale bar: 10 µm. I) CLSM images showing the endocytosis of BP-Cy5 in SH-SY5Y cells after incubation with various inhibitors. Scale bar: 50 µm. J) Colocalization of Cy5 and BP-Cy5 with the ER, Lyso, and Mito in SH-SY5Y cells visualized using CLSM. Scale bar: 10 µm. Quantitative comparison of fluorescence intensity of BP-Cy5 in K) HNEpC and L) SH-SY5Y cells following incubation with various inhibitors ($n = 3$). **$p < 0.01$ and ***$p < 0.001$ versus the control group. Pearson's correlation coefficient between Cy5 and BP-Cy5, and the ER, Lyso, and Mito, in M) HNEpC and N) SH-SY5Y cells, measured using ImageJ software ($n = 3$). Data in (B–D) and (K–N) were processed using GraphPad Prism 8.0 and are presented as the mean ± SD. The *p*-values were determined using one-way ANOVA with Tukey's post-hoc test.

© 2024 Wiley-VCH GmbH

Downloaded for personal academic use. All rights reserved. https://papernode.online/

caveolae-mediated endocytosis was also involved. During intracellular trafficking, BP-Cy5 was found to be transported to lysosomes, ER, and mitochondria. Then, it followed the ER–Golgi complexes–basolateral membrane route and was excreted out.

The cellular uptake of BP-Cy5 by SH-SY5Y cells was then investigated. As illustrated in Figure 4I, all inhibitors suppressed the internalization of BP-Cy5 to various degrees. HS treatment triggered the greatest attenuation of intracellular fluorescence signals (81%), followed by CPZ (54.2%), EIPA (36%), and MβCD (23.8%), indicating that the uptake of BP-Cy5 largely occurred via clathrin-mediated endocytosis (Figure 4L). In addition, EIPA and MβCD also decreased the cellular uptake of BP-Cy5, revealing the roles of macropinocytosis and caveolae endocytosis.

To examine intracellular trafficking in SH-SY5Y cells, confocal micrographs and corresponding Pearson's correlation analysis were obtained (Figure 4J,N). The ER is involved in the trafficking of intracellular cargo. In line with this, both Cy5 and BP-Cy5 showed the highest PCC with ER (0.7 for Cy5 and 0.55 for BP-Cy5), indicating that large amounts of Cy5 and BP-Cy5 were transported to the ER. Moreover, the PCC of Cy5 (0.51) and BP-Cy5 (0.46) with Mito revealed that a fair percentage of these materials also accumulated in the mitochondria. Since the pathogenesis of AD is inextricably linked to mitochondrial dysfunction, we speculated that the mitochondrial distribution of drugs would help in regulating mitochondrial function post-treatment. In addition, the lowest PCC was observed between Lyso and Cy5 (0.25), demonstrating that only a small proportion of Cy5 was transported into lysosomal compartments. In contrast, BP-Cy5 exhibited higher accumulation in Lyso (PCC = 0.48) than free Cy5 (Figure 4N). The cellular endocytosis pathway and transport of BP-Cy5 in SH-SY5Y cells are summarized in Figure 4F.

Timely lysosome escape is crucial for preserving the pharmacological activity of endocytosed nanomedicines. We further investigated the lysosome escape of BP-Cy5 in SH-SY5Y cells. Fluorescence images and correlations between BP-Cy5 and Lyso as a function of incubation time are shown in Figure S15, Supporting Information. The PCC values at 1, 2, and 4 h post-treatment were 0.52, 0.51, and 0.52, respectively. These results indicated that the accumulation of BP-Cy5 in lysosomes occurs very soon, within the first 1 h, and is maintained for at least 4 h.

2.5. BP-MB Alleviated Neuronal Damage In Vitro

Hyperphosphorylated tau can induce oxidative stress and impair mitochondrial function, subsequently causing caspase-dependent neuronal apoptosis.[7a] To evaluate the antioxidative and neuroprotective ability of BP-MB, we first studied the cytotoxicity of different formulations against SH-SY5Y cells. As presented in **Figure** 5A, the cell viability of the MB, BP, and BP-MB groups at various concentrations all exceeded 87.55%, indicating the good compatibility of these agents. In addition, we tested the compatibility of these formulations in bEnd. 3 cells and RAW 264.7 cells (Figure S16, Supporting Information). Minimal cytotoxicity was observed with various concentrations of BP and BP-MB, while 16 μg mL^{-1} MB exhibited obvious cytotoxicity in RAW 264.7 cells.

OA is a potent inhibitor of protein phosphatase PP-1 and PP-2A and has been widely used for inducing tau-related AD pathogenesis. [33]Thus, we constructed a tauopathy-like cellular model by treating SH-SY5Y cells with OA. At concentrations of 40 nM or higher, OA was highly cytotoxic to SH-SY5Y cells (Figure 5B). In order to ensure the achievable rescue effects, we selected 40 nM OA for subsequent modeling. Cells were incubated with MB, BP, or BP-MB for 24 h after OA pretreatment. As shown in Figure 5C, MB attenuated the cytotoxicity of OA in SH-SY5Y cells at 2 μg mL^{-1}, with the cell viability increasing from 50.44% to 63.35%. With its antioxidant activity, BP exhibited obvious anti-apoptotic effects at 5 μg mL^{-1}. Moreover, 10 μg mL^{-1} of BP-MB exerted excellent synergistic protective effects, elevating cell viability to 85.10%, significantly higher than BP (77.07%) or MB (63.35%) alone.

Subsequently, flow cytometry analysis was also executed for apoptosis analysis based on Annexin V-FITC staining (Figure S17, Supporting Information). OA treatment led to a cell apoptosis rate of 47.56%, but BP-MB intervention (10 μg mL^{-1}) strongly alleviated cell damage, causing the cell apoptosis rate to 11.74%. Its effects were better than those of MB treatment (18.2% apoptosis) and BP treatment (22.22%) alone. These results suggested that BP-MB could effectively rescue neurons from OA-induced death.

Studies have demonstrated that hyperphosphorylated tau, microtubule disorder, and NFTs can promote ROS generation, subsequently causing neuronal death.[26] Therefore, we assessed the anti-oxidative ability of BP-MB in an OA-induced cell model. Cellular ROS levels were detected by flow cytometry using a ROS-sensitive dye, dichlorodihydrofluorescein diacetate (DCFH-DA). OA treatment generated a large amount of ROS in treated cells. By contrast, the ROS content in all treatment groups showed a decreasing trend, and the ROS level was lowest in cells subjected to 10 μg mL^{-1} BP-MB. This may be due to the synergistic therapeutic effect achieved by combining the antioxidative activities of MB and BP (Figure S18, Supporting Information). MB has been reported to accumulate within mitochondria, improve mitochondrial respiration, and inhibit superoxide production.[34] Thus, MB was also expected to inhibit mitochondrial ROS in this study. We explored the mitochondrial ROS scavenging capability of BP-MB using a MitoSox kit in which the fluorescence intensity represents mitochondrial ROS accumulation. As shown in Figure 5G, OA-treated cells exhibited strong fluorescence. Comparatively, the MB group showed remarkably lower fluorescence intensity levels, while BP-MB demonstrated the best mitochondrial ROS inhibition efficacy. It was also verified by the quantification of the mean fluorescence intensity (MFI) of mitochondrial ROS (Figure S19, Supporting Information).

Elevated ROS levels cause mitochondria to produce proapoptotic proteins and finally induce neuronal apoptosis.[35] A decline in mitochondrial membrane potential (MMP) reflects the activation of the mitochondrial apoptosis pathway.[36] Thus, we detected the MMPs of SH-SY5Y cells subjected to different treatments using JC-1 staining. As shown in Figure S20, Supporting Information, compared with non-treated cells, cells treated with OA showed a higher proportion of P2 (green fluorescence monomers; increased to 42.5%), reflecting the lower MMP due to mitochondrial damage. However, 10 μg mL^{-1} BP-MB significantly attenuated the damage in OA-treated cells, as evidenced by the decreased proportion of P2 (reduced to 13.12%). These

© 2024 Wiley-VCH GmbH

Downloaded for personal academic use. All rights reserved. https://papernode.online/

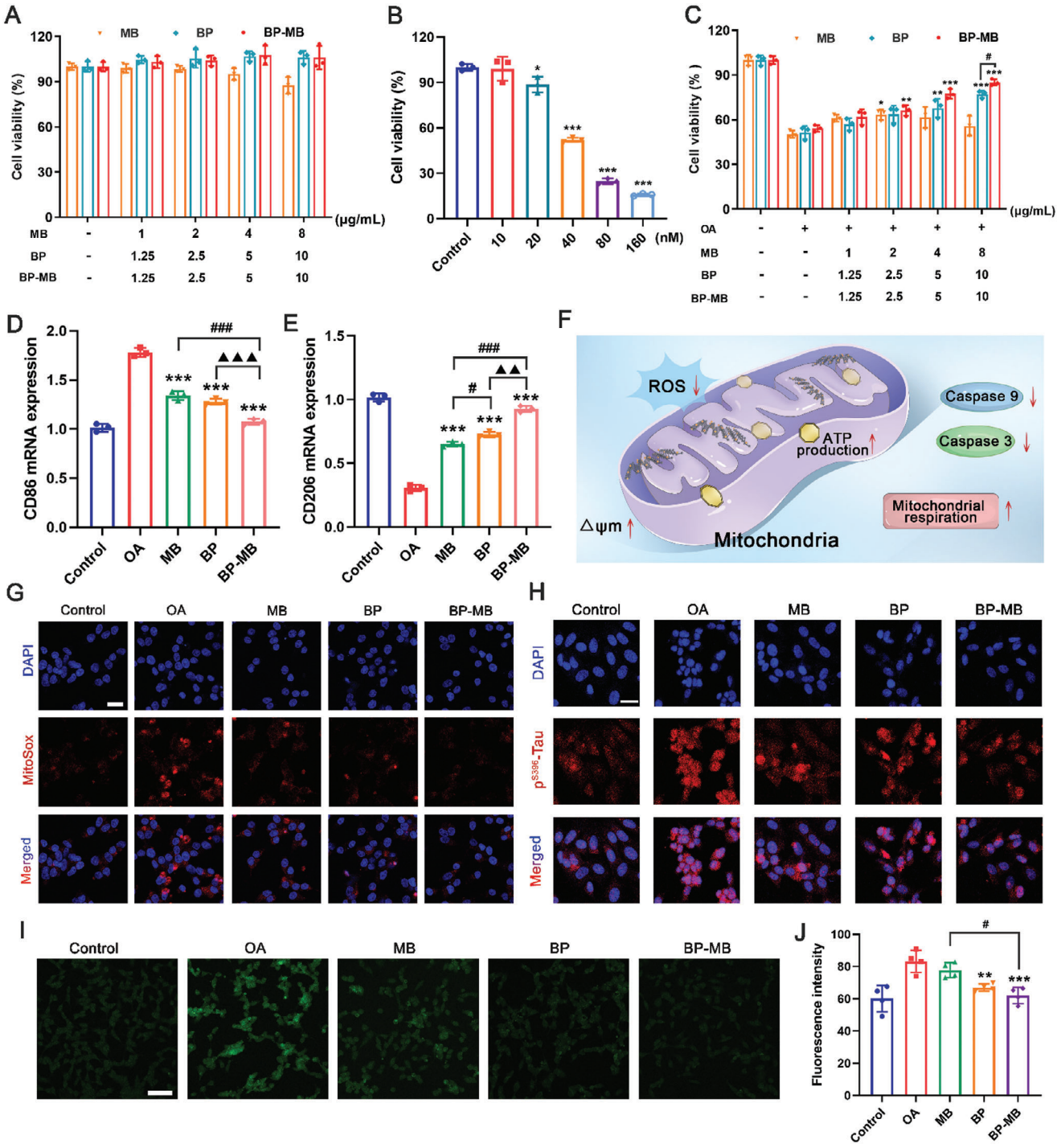

Figure 5. BP-MB protected neurons from OA-induced damage. A) Cytotoxicity measurement in SH-SY5Y cells following various treatments ($n = 3$). B) Cell viability of SH-SY5Y cells treated with different concentrations of OA ($n = 3$). $^{*}p < 0.05$ and $^{***}p < 0.001$ versus the control group. C) Cell viability of OA-pretreated SH-SY5Y cells subjected to different treatments ($n = 3$). $^{*}p < 0.05$, $^{**}p < 0.01$, and $^{***}p < 0.001$ versus the OA group. $^{\#}p < 0.05$ versus the BP group. The mRNA levels of D) CD86 and E) CD206 in OA-pretreated BV2 cells following the indicated treatments ($n = 3$). $^{***}p < 0.001$ versus the control group. $^{\#}p < 0.05$, $^{\#\#\#}p < 0.001$ versus the MB group. $^{\blacktriangle\blacktriangle}p < 0.01$, $^{\blacktriangle\blacktriangle\blacktriangle}p < 0.001$ versus the BP group. F) Mechanism underlying the restoration of mitochondrial function following BP-MB treatment. G) Mitochondrial ROS levels detected using the MitoSox probe. Scale bar: 50 μm. H) Confocal fluorescence images of p-tau (S396) in SH-SY5Y cells. Scale bar: 25 μm. I) Representative fluorescence images of tau aggregation examined using the ThS probe. Scale bar: 50 μm. J) Quantification of the mean fluorescence intensity (MFI) of ThS in OA-pretreated SH-SY5Y cells subjected to different treatments ($n = 3$). $^{**}p < 0.01$ and $^{***}p < 0.001$ versus the OA group. $^{\#}p < 0.05$ versus the MB group. Data in (A–E) and (J) were processed on GraphPad Prism 8.0 and are presented as the mean ± SD. The p-values were determined using one-way ANOVA with Tukey's post-hoc test.

© 2024 Wiley-VCH GmbH

Downloaded for personal academic use. All rights reserved. https://papernode.online/

results indicated that BP-MB could effectively inhibit impairments to the mitochondrial membranes of neurons.

2.6. BP-MB Restored the Mitochondrial Function of Neurons

Mitochondrial damage can be induced by pathogenic tau and ROS elevation, aggravating AD pathology.[37] Hence, we hypothesized that BP-MB could restore the mitochondrial function of neurons by reducing oxidative stress. Therefore, seahorse experiments were executed and the effects of BP-MB on mitochondrial respiration were examined. Oxygen consumption rate (OCR) is an indicator of mitochondrial oxidative respiration,[38] and it is measured by treating SH-SY5Y cells with oligomycin (an ATP synthase inhibitor), FCCP (an agent uncoupling the mitochondrial electron transport chain), and a mixture of rotenone and antimycin A (an inhibitor of mitochondrial complex III and I) one after the other (Figure S21, Supporting Information). In comparison with the control group, cells treated with OA exhibited significant OCR inhibition, as indicated by reduced basal respiration, ATP production, H^+ proton leak, and maximum respiration levels. However, cells treated with BP-MB exhibited the most remarkable improvements in these energy indicators (Figure S22, Supporting Information), demonstrating that BP-MB could ameliorate the dysfunction of mitochondrial respiration in cellular AD models.

Mitochondrial dysfunction can activate the caspases, leading to apoptotic cell death.[39] Thus, we further assessed the role of BP-MB in mitochondrial protection by analyzing the expression levels of caspase 3 and caspase 9. As evidenced in Figure S23A,B, Supporting Information, OA exposure significantly up-regulated caspase 3 and caspase 9 levels in treated cells. As expected, BP-MB treatment obviously reduced the levels of these two caspases, and these findings were confirmed by quantified analyses (Figure S23C,D, Supporting Information). Collectively, this evidence demonstrated that BP-MB could reduce ROS content, rescue mitochondrial dysfunction, and down-regulate caspase protein expression, thereby alleviating neuronal damage (Figure 5F).

2.7. BP-MB Modulates Neuroinflammation and Inhibits p-Tau Aggregation

Microglia play a crucial role in the regulation of neuroinflammation and brain repair by switching between an anti-inflammatory and pro-inflammatory state. ROS overproduction may promote microglial polarization toward the M1 phenotype.[40] To investigate the effect of BP-MB on microglial polarization, the mRNA expression of *CD86* (M1 marker) and *CD206* (M2 marker) was evaluated using RT-qPCR. OA pre-treatment induced the proinflammatory transformation of BV-2 cells, as evidenced by increased *CD86* and decreased *CD206* levels. By contrast, the expression of CD86 was remarkably reduced after treatment with BP-MB. Meanwhile, the levels of the M2 marker *CD206* were increased following the BP-MB treatment (Figure 5D,E). These results suggested that BP-MB could modulate microglia-induced neuroinflammation for AD therapy.

Hyperphosphorylated tau tends to aggregate intracellularly and forms NFTs that can damage neurons.[41] Herein, the levels of hyperphosphorylated tau were estimated based on immunofluorescence staining. As shown in Figure 5H and Figure S24, Supporting Information, the highest fluorescence intensity of p-Tau S396 was observed in OA-treated cells, demonstrating the up-regulation of cellular tau phosphorylation. However, the fluorescence signals were negligible in the cells treated with BP-MB, illustrating its effectiveness in inhibiting tau phosphorylation. We then performed a Thioflavin S (ThS) fluorescence assay to detect the degree of tau aggregation. As shown in Figure 5I,J, the fluorescence intensity of OA-stimulated cells increased significantly when compared with the control group, suggesting that OA could induce tau aggregation. However, the ThS signal was weakened after incubation with MB due to its inhibitory effects on tau-tau interaction.[42] BP also induced an obvious decrease in fluorescence intensity, which could be ascribed to its antioxidant activities, while BP-MB displayed the most marked reduction in ThS fluorescence intensity. This proved that the tau aggregation was effectively constrained following BP-MB treatment.

2.8. Brain Accumulation and Pharmacokinetics In Vivo

IN administration enables the direct delivery of drugs from the nose to the brain, bypassing the BBB (**Figure 6**A). Hence, to evaluate drug accumulation in the brain, we detected the fluorescence intensity of free Cy5, BP-Cy5, and BP-Cy5@Gel in the mouse brain at designated time points following IN administration. A fluorescence signal was clearly visible in all treatment groups after 1 h. Moreover, free Cy5 showed the strongest fluorescence intensity after 2 h, but it was gradually metabolized and became undetectable after the 4 h time point. The strongest fluorescence intensity for BP-Cy5 was observed at 4 h, while BP-Cy5@Gel took a longer time to reach peak accumulation in the brain (6 h). This could be attributed to the sustained drug release effect of the hydrogel. Compared with BP-Cy5, BP-Cy5@Gel exhibited significantly higher accumulation in the brain at 6 h and maintained this advantage even at 24 h (Figure S25, Supporting Information). These results were validated using fluorescence quantitative analysis (Figure 6B). Above all, these results proved that BP-Cy5@Gel could prolong nasal drug retention to sustain the drug release for brain-targeted delivery. Hence, we further investigated the fluorescence distribution of BP-Cy5@Gel in different brain regions. As shown in Figure 6C, the fluorescence signal was more concentrated in the hippocampus and entorhinal cortex, while the enrichment in the periaqueductal gray was limited. In fact, the fluorescence signal was 10.34-fold and 12.30-fold higher in the hippocampus and entorhinal cortex than in the periaqueductal gray, respectively (Figure 6D). Since dysfunction within the hippocampus and entorhinal cortex was closely linked to cognitive impairment in AD,[43] and NFTs were most frequently found in these two regions,[44] drug accumulation in these sites could facilitate AD treatment.

We subsequently performed a pharmacokinetic study to analyze MB levels in the plasma and brain post the intravenous (IV) or IN administration of different formulations. The critical pharmacokinetic parameters were calculated and given in Tables S3 and S4, Supporting Information. The plasma concentration-time profiles following IV administration and IN administration are shown in Figure 6E,F, respectively. Rats administrated

© 2024 Wiley-VCH GmbH

Downloaded for personal academic use. All rights reserved. https://papernode.online/

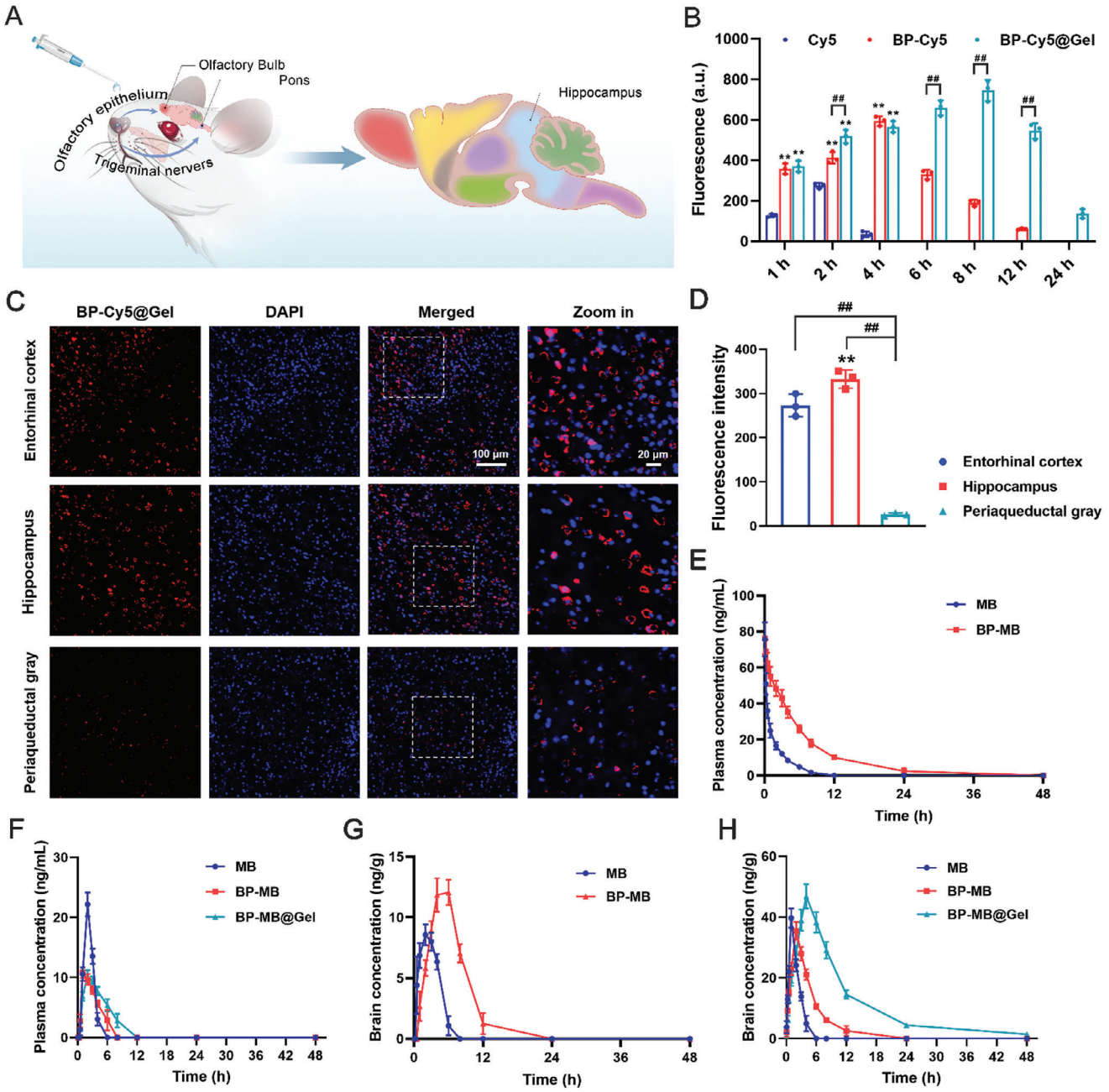

Figure 6. Brain accumulation and pharmacokinetics of formulations following IN administration. A) Schematic illustration of the IN administration of BP-MB@Gel. B) Quantitative analysis of fluorescence intensity in the brain ($n = 3$). $^{*}p < 0.05$ versus the Cy5 group. $^{\#\#}p < 0.01$ versus the BP-Cy5 group. C) Representative confocal images of fluorescence distribution in different brain regions following IN administration of BP-Cy5@Gel. Scale bar: 100 μm and 20 μm for magnified images. D) Quantitative analysis of fluorescence intensity in the indicated mouse brain regions (n=3). **E–H) Plasma MB concentration versus time curves following E) IV administration and F) IN administration. Brain MB concentration versus time curves following G) IV administration and H) IN administration. Data in (B) and (D–H) were processed on GraphPad Prism 8.0 and are presented as the mean ± SD. The p-values were determined using one-way ANOVA with Tukey's post-hoc test.

with MB and BP-MB intravenously showed a time-dependent manner decrease in plasma MB levels. Although free MB was only detectable during the first 8 h, BP-MB treatment prolonged MB circulation to 24 h. Moreover, the area under the plasma concentration-time curve from 0 to t (AUC_{0-t}) value of BP-MB was 4.13-fold that of the MB solution. Following IN administration, as seen in Figure 6F, free MB was the first to achieve its peak concentration (22.17 ± 1.98 ng mL^{-1}). However, its levels quickly decreased and became very low by 4 h. By contrast, the BP-MB@Gel group exhibited a longer systemic circulation life (12 h) and a significantly longer half-life ($T_{1/2}$) (3.80 ± 0.36 h vs 0.71 ± 0.11 h). Moreover, the AUC_{0-t} of BP-MB@Gel (50.91 ±

© 2024 Wiley-VCH GmbH

Downloaded for personal academic use. All rights reserved. https://papernode.online/

4.66 ng h mL^{-1}) was also higher than that of MB (46.08 ± 4.31 ng h mL^{-1}) and BP-MB (39.12 ± 3.58 ng h mL^{-1}). Consistently, a higher mean residence time (MRT_{0-t}) value was observed in the BP-MB@Gel group (3.68 ± 0.35 h) than in the MB (2.16 ± 0.24 h) and BP-MB groups (2.63 ± 0.27 h). These results demonstrated that the BP-MB@Gel system provided sustained and controlled drug release behavior, which facilitated an enhancement of drug efficacy.

The IN route is useful for brain-targeted delivery.[45] Therefore, we assessed whether nasal administration could provide better MB distribution in the brain than the IV route. As seen in Figure 6G,H, free MB was metabolized rapidly from the brain within 6 h after IV and IN administration. By contrast, BP-MB could prolong brain retention and enhance the bioavailability of MB, leading to significantly higher $MRT_{0\text{-}t}$ (5.44 ± 0.56 h for IV; 3.84 ± 0.43 for IN) and AUC_{0-t} (83.74 ± 7.88 ng h mL^{-1} for IV; 535.46 ± 56.39 ng h mL^{-1} for IN). Meanwhile, the hydrogel would undergo sol–gel transition in the nasal cavity, thus increasing drug residence time and releasing the drug sustainably.[46] Therefore, we speculated that IN BP-MB@Gel could improve the efficiency of brain-targeted delivery. IN BP-MB@Gel took the longest time to reach its maximum brain concentration (T_{max}) and peak brain concentration (C_{max}), and the drug retention time in the brain was up to 48 h post-IN administration (Figure 6H). The $T_{1/2}$ value in the BP-MB@Gel group (5.83 ± 0.61 h) was remarkably longer than that after IV (1.80 ± 0.15 h) or IN treatment (2.63 ± 0.28 h) with BP-MB (Tables S3 and S4, Supporting Information). Moreover, the C_{max} of the brain MB in the BP-MB@Gel group was 3.88 times that of the BP-MB IN group (46.81 ± 4.01 vs 12.06 ± 1.04 ng mL^{-1}), and BP-MB@Gel required a longer time to reach peak MB levels (4.89 ± 0.51 vs 6.51 ± 0.58 h). Notably, the brain AUC_{0-t} value of BP-MB@Gel was 535.46 ± 56.39 ng h mL^{-1}, which was 3.23-fold and 6.39-fold higher than that of BP-MB administered via the IN and IV routes, respectively. Furthermore, the $MRT_{0\text{-}t}$ of BP-MB@Gel (10.76 ± 1.21 h) was also much longer than that of free MB (2.59 ± 0.24 h for IV; 1.93 ± 0.22 h for IN) and BP-MB group (5.44 ± 0.56 for IV; 3.84 ± 0.43 for IN). Interestingly, the AUC_{0-t} values for the BP-MB group and BP-MB@Gel group were both remarkably higher in the brain than in the plasma after IN administration, indicating that most of the MB was transported to the brain and only a small portion reached the systemic circulation. Notably, BP-MB@Gel showed the highest AUC_{brain}/AUC_{plasma} ratio. Moreover, its DTE% and DTP% values were calculated to be 54.79% and 98.55%, respectively. Altogether, the above results verified that the nasal delivery of BP-MB@Gel provided the advantages of enhancing the accumulative brain distribution of MB and prolonging drug residence duration to realize the long-term treatment of AD.

2.9. BP-MB@Gel Rescued the Cognitive Decline in AD Model Mice

The pathogenic tau protein can spread from a diseased neuron to a healthy one in a "prion-like" manner,[47] leading to diffused neurodegeneration in the brain. Injecting OA into the amygdala was reported to induce a rapid spread of phosphorylated tau protein and result in tau protein aggregation.[48] Herein, we used OA to develop a tau-related mouse model of AD and assess the neuroprotective efficacy of BP-MB@Gel in vivo. The treatment schedule is illustrated in **Figure** 7A. A series of behavior tests were implemented to evaluate memory and cognition in AD mice following the IN administration of various formulations.

In the Morris water maze (MWM) test, representative swimming paths for each group are displayed in Figure 7B. Compared with the control group, the OA-induced AD group exhibited spatial learning impairments, which presented a significant increase in escape latency from the fourth day of the acquisition period. By contrast, mice in the treatment groups, especially the BP-MB@Gel group, all exhibited a decreasing trend of escape latency (Figure 7C). Since mice with good retention abilities exhibited spatially oriented swimming behavior instead of wandering around, their swimming distances were also shorter than those of the OA group (Figure S26, Supporting Information). In the probe trial, as indicated by the swimming path in **Figure** 8B, tauopathy mice performed poorly during the platform search. They spent much less time in the target quadrant and exhibited fewer platform crossings than the control group (Figure 7D,E). However, mice in the BP-MB@Gel group preferentially moved toward the initial platform area, showing the longest time in the target quadrant and the highest frequency of platform crossings among the treatment groups. These results verified that BP-MB@Gel exerted the most prominent effects for attenuating spatial memory deficits in AD mice.

Nest-building behavior can be impacted due to hippocampal damage and neurodegenerative disease.[49] Therefore, the nesting performance of mice was also evaluated in this study. As shown in Figure 7F, the nest constructed by OA-treated mice was made up of partially torn material, and the material was not gathered into a nest but rather spread around the cage. This was indicative of impaired nesting behavior. By contrast, BP-MB@Gel treatment remarkably improved nesting scores (Figure 7G). These mice had an identifiable nest with walls higher than the height of the mouse. Consistent with the results obtained from the MWM test, BP-MB@Gel treatment also attenuated the cognitive declines.

The open-field test was conducted to investigate the locomotor activity and exploratory behavior of mice. In a new open environment, mice tend to travel around the periphery due to fear, and this behavior is particularly evident in mice with anxiety. The exploratory trajectory of mice in this study (Figure S27A, Supporting Information) showed that OA-treated mice tended to stay away from the central area, spent less time in the central zone, and had a shorter movement distance than the normal control group (Figure S27B,C, Supporting Information). Hence, they showed heightened anxiety levels and lower exploratory desires. Nevertheless, BP-MB@Gel treatment ameliorated the anxiety-related behaviors of mice, providing the best effects, as evidenced by the increased travel path length and the time spent in the central area. Moreover, the total locomotor activity was also improved following BP-MB@Gel treatment as well (Figure S27D, Supporting Information).

Finally, five-choice serial reaction-time (5-CSRT) task touchscreen experiments were performed to test attention and executive functioning in rodents, which depends on GABAergic systems in the medial prefrontal cortex.[50] The stages for 5-CSRT task trainning were displayed in Table S5, Supporting Information. As illustrated inFigure 8H, in the task, mice who nose-poked

© 2024 Wiley-VCH GmbH

Downloaded for personal academic use. All rights reserved. https://papernode.online/

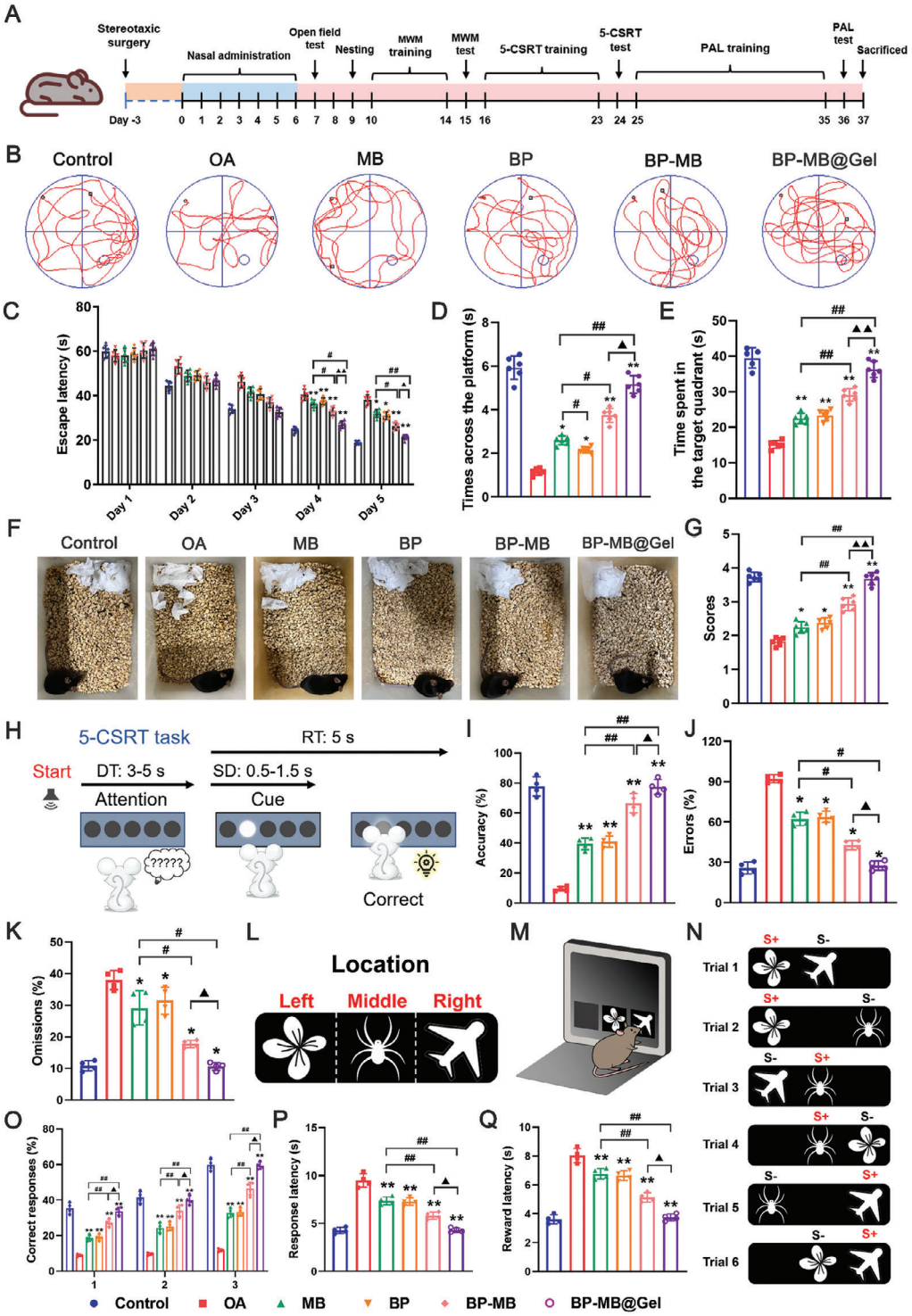

Figure 7. Behavioral evaluation of AD model mice following BP-MB@Gel therapy. A) Schedule of drug treatment and behavioral tests. B) Representative swimming paths for each group in the Morris water maze. C) Mean escape latency, D) frequency of crossing of the initial platform, and E) swimming time in the targeted quadrant in all groups of treated mice ($n = 6$). F) Representative images and G) scores for nesting behavior on day 3 ($n = 6$). H) Schematic depicting the 5-CSRT task. DT, delay time; SD, stimulus time; RT, reaction time. I) Accuracy (percent correct), J) the percentage of errors (incorrect + omissions), and K) the percentage of omissions in the 5-CSRT task ($n = 4$). L) Correct location of each stimulus on the screen. M) Schematic illustration of the PAL task. N) PAL test with six possible trial types (S+, correct; S−, incorrect). O) Percentage of correct responses across blocks of trials in the PAL task. P) Latency (s) to respond to a stimulus and Q) latency (s) to collect food reward ($n = 4$). $^{*}p < 0.05$ and $^{**}p < 0.01$ versus the OA group. $^{\#}p < 0.05$ and $^{\#\#}p < 0.01$ versus the MB group. $^{\blacktriangle}p < 0.05$ versus the BP-MB group. Data in (C–E), (G), (I–K), and (O–Q) were processed on GraphPad Prism 8.0 and are presented as the mean ± SD. The *p*-values were determined using one-way ANOVA followed by Tukey's post-hoc test.

© 2024 Wiley-VCH GmbH

Downloaded for personal academic use. All rights reserved. https://papernode.online/

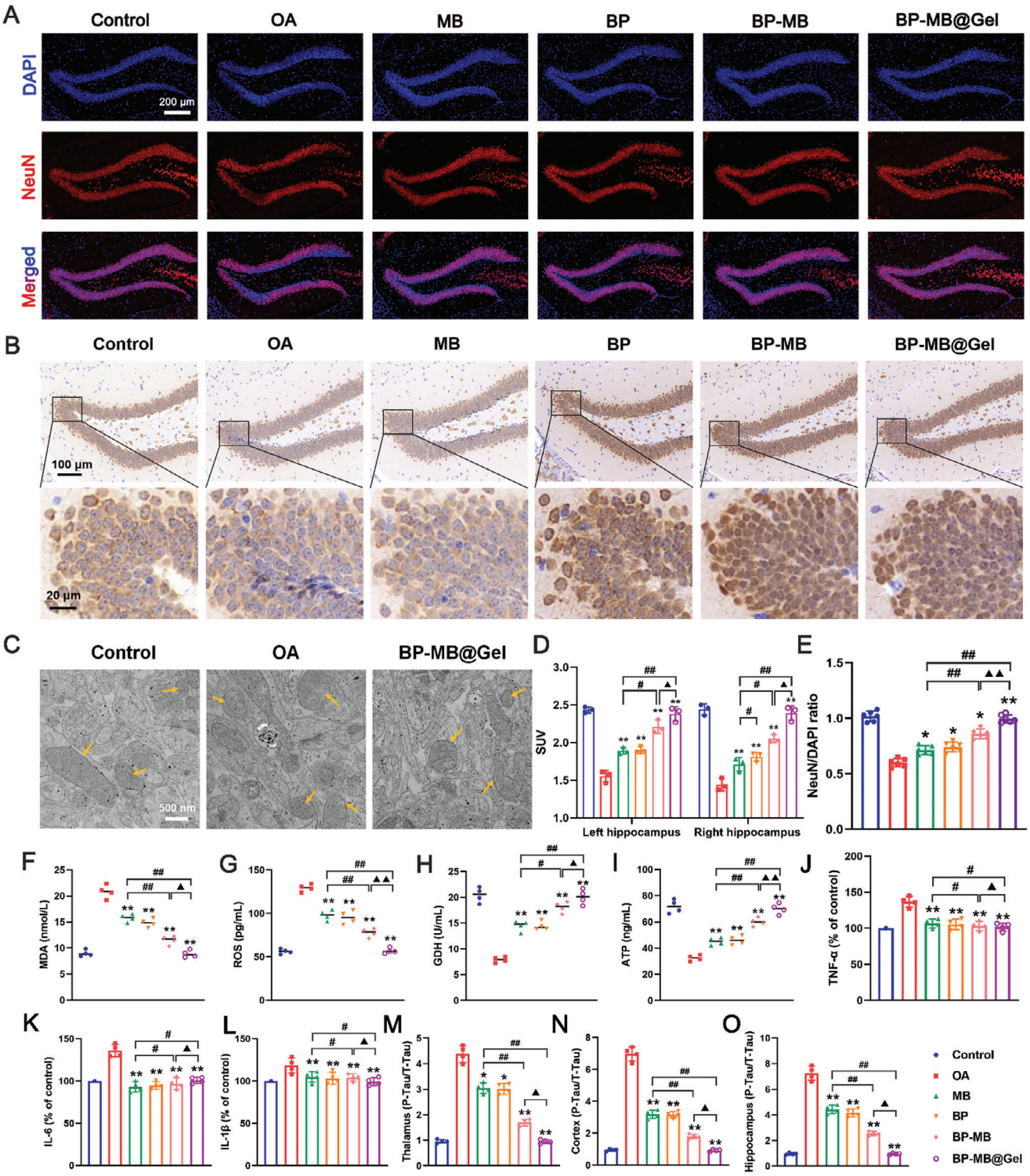

Figure 8. BP-MB@Gel attenuated neuronal damage and relieved p-tau burden in vivo. A) Immunostaining of NeuN-positive cells (red) in the hippocampal DG. Scale bar: 200 μm. B) Representative images of H&E staining in the DG. Scale bar: 100 and 20 μm for magnified images. C) Ultrastructure of hippocampal mitochondria observed using Bio-TEM. Scale bar: 500 nm. D) Quantitative analysis of [^{18}F]-FDG uptake in the left and right hippocampal regions ($n = 3$). E) Quantitative analysis of the NeuN/DAPI ratio ($n = 6$). Contents of F) MDA, G) ROS, H) GDH, and I) ATP in the hippocampus ($n = 4$). MDA, malondialdehyde; ROS, reactive oxygen species; GDH, glutamate dehydrogenase; ATP, adenosine triphosphate. Levels of proinflammatory cytokines such as J) tumor necrosis factor-α (TNF-α), K) interleukin 6 (IL-6), and L) interleukin 1β (IL-1β) in the hippocampus ($n = 4$). ELISA analysis of p-tau levels in the M) thalamus, N) cortex, and O) hippocampus ($n = 4$). $^{*}p < 0.05$ and $^{**}p < 0.01$ versus the OA group. $^{\#}p < 0.05$ and $^{\#\#}p < 0.01$ versus the MB group. $\blacktriangle p < 0.05$ and $\blacktriangle\blacktriangle$ $p < 0.01$ versus the BP-MB group. Data in (D–O) were processed on GraphPad Prism 8.0 and are presented as the mean ± SD. The p-values were determined using one-way ANOVA followed by Tukey's post-hoc test.

© 2024 Wiley-VCH GmbH

Downloaded for personal academic use. All rights reserved. https://papernode.online/

a visual stimulus at the right location within a reaction time (RT) of 5 s received a reward. Meanwhile, incorrect responses (nose-poking wrong stimulus location) and omissions (failing to indicate stimulus location within RT) were scored as errors and considered as results of impaired concentration.[51] After training, the performance of mice in the BP-MB@Gel group (accuracy at 2-s stimulus time [SD]) became similar to that of controls. However, OA-treated mice displayed poorer accuracy and made more omissions and erroneous responses (Figure 7I–K). This revealed that attention deficits in AD model mice were effectively improved by BP-MB@Gel treatment. Another touchscreen test, the paired associate learning (PAL) task, was conducted to test the cognitive capability of the mice.[52] As shown in Figure 8L,M, the mice were required to learn and recall multiple objects (flower, spider, and plane) associated with one of three locations on the touch screen (left, middle, and right, respectively).[53] The possible trial types are listed in Figure 7N. The control group (normal mice) exhibited progressive improvements in accuracy across various blocks of training trials, giving around 60% correct response by the end of training. In comparison, OA-treated mice maintained a significantly lower accuracy of <12% across training, suggesting a severe impairment of object-location PAL. Similar to the controls, mice in the BP-MB@Gel group progressively acquired associative learning, indicating that BP-MB@Gel treatment could reverse cognitive impairment in AD mouse models (Figure 7O). Finally, control mice exhibited the shortest response latency and reward latency among all groups. Although OA-treated mice displayed the longest response latency to both stimulus and food reward collection, BP-MB@Gel-treated mice responded as rapidly as control mice (Figures 7P and 8Q).

2.10. BP-MB@Gel Restored the Brain Function

Decreased cerebral glucose uptake has been shown to compromise neuronal function and health, and hippocampal glucose metabolic disorder was associated with learning and memory deficits.[54] Therefore, in this study, 2-deoxy-2-(^{18}F) fluoro-D-glucose (^{18}F-FDG-PET) was used as a contrast agent for positron emission tomography (PET) imaging to reveal brain glucose uptake in mice.

A significant decrease in FDG-PET signals was detected in AD models, suggestive of abnormal cerebral glucose utilization. However, this metabolic depression was attenuated in the brains of AD mice after treatment with different formulations, and mice treated with BP-MB@Gel showed a homogenous signal distribution and the highest FDG uptake in all brain regions (Figure S28, Supporting Information). We further quantified hippocampal FDG uptake based on calculated standardized uptake values (SUVs). As depicted in Figure 8D, relative to OA-induced mice, the BP-MB@Gel group showed much higher glucose uptake in both the left and right hippocampus (2.38 ± 0.16 and 2.39 ± 0.15, respectively). Moreover, these values were comparable to those in the control group (2.43 ± 0.18 and 2.44 ± 0.16, respectively). The findings implied that BP-MB@Gel had a positive impact on energy metabolism and neuronal function in the brain.

Next, to investigate whether BP-MB@Gel treatment could attenuate neuronal impairment, the expression of the neuronal marker NeuN was analyzed in the hippocampus. Massive neuron loss was observed in the OA group, with a noticeably reduced density of NeuN-positive (red) cells. After treatment with MB, BP, BP-MB, and BP-MB@Gel, the number of neurons increased in mice, albeit to various degrees (Figure 8A). Notably, BP-MB@Gel treatment provided the highest NeuN/DAPI ratio (Figure 8E), implying that BP-MB@Gel administration could exert better neuroprotective effects than any other treatment. Furthermore, hematoxylin and eosin (H&E) staining was performed to stain nerve cells, and obvious neuronal damage characterized by cell shrinkage and nuclear pyknosis was observed in the hippocampal dentate gyrus (DG) in AD model mice. However, such damage was prominently alleviated following BP-MB@Gel treatment (Figure 8B). Taken together, these results suggested that BP-MB@Gel could provide better neuronal protection than other formulations in vivo.

Abnormal mitochondrial morphology is suggestive of functional deficits, and previous studies have shown that OA interventions cause mitochondrial dysfunction and induce memory loss in rats.[55] Therefore, the ultrastructural morphology of mitochondria was detected under the biological TEM (Bio-TEM) in this study. As depicted in Figure 8C, OA treatment caused severe cristae disruptions and membrane damage in mitochondria. By contrast, the mitochondria in the BP-MB@Gel group exhibited healthy morphology with normal cristae and an intact membrane, suggesting that BP-MB@Gel treatment could maintain the structural and functional integrity of mitochondria. Given that compromised mitochondrial function is often associated with increased oxidative damage,[56] we next measured a series of oxidation-related indicators in the treatment groups. Malondialdehyde (MDA) (the product of lipid peroxidation) and ROS levels were significantly higher in AD model mice than in the control group. However, their levels were inhibited to a certain extent after treatment with various formulations and returned to near-normal in BP-MB@Gel-treated mice (Figure 8F,G). Glutamate dehydrogenase (GDH), a mitochondrial matrix enzyme that plays an important role in energy homeostasis, and is dysregulated under conditions of AD pathology,[57] showed reduced activity in the OA group. However, GDH activity was recovered after BP-MB@Gel treatment, reaching levels comparable to those of the control group (Figure 8H). Similarly, increased ATP production was detected in BP-MB@Gel-treated AD model mice (Figure 8I).

In the hippocampus, representative inflammatory mediators, such as tumor necrosis factor-α (TNF-α), interleukin 1β (IL-1β), and interleukin 6 (IL-6), showed 36%, 18%, and 30% higher levels in OA-treated mice than controls, respectively. However, BP-MB@Gel treatment reduced these proinflammatory cytokines to normal levels (Figure 8J–L). Finally, we evaluated the mitigatory effects of BP-MB@Gel treatment on p-tau burden using an ELISA kit.[58] As demonstrated in Figure 8M–O, the ratio of p-tau/total tau (T-tau) was remarkably increased in the thalamus, cortex, and hippocampus in the OA group when compared with the control group, indicating the development of a tau pathology animal model. Contrastingly, the expression of p-tau was prominently downregulated in all treatment groups, with BP-MB@Gel showing the strongest efficacy. Collectively, this showed that BP-MB@Gel administration exerted neuroprotective effects by regulating mitochondrial function, relieving neuroinflammation, and reducing p-tau levels.

© 2024 Wiley-VCH GmbH

Downloaded for personal academic use. All rights reserved. https://papernode.online/

2.11. In Vivo Biocompatibility

Drugs used for AD treatment must possess good biocompatibility. Hence, we evaluated the biocompatibility profiles of BP-MB@Gel in our mouse models. There was no obvious alteration of routine blood biomarkers and biochemistry parameters between the control and treatment groups (Figures S29 and S30, Supporting Information). Additionally, the organ indexes for the heart, liver, spleen, lung, and kidney were within the normal range relative to the control group in all treatment groups (Figure S31, Supporting Information). Tissue sections of the nasal mucosa and major organs were examined using H&E staining, and no evidence of tissue inflammation or damage was observed (Figures S32 and S33, Supporting Information), indicating that none of the formulations cause an inflammatory response in vivo following IN injection. To examine whether drug accumulation in the brain potentially caused side effects such as cerebral thrombosis, nuclear magnetic resonance imaging (MRI) was conducted. No anomalies in the brain were detected on T2-weighted images (Figure S34, Supporting Information). Together, these results verified that intranasally administered BP-MB@Gel possessed desirable biocompatibility, ensuring the safety of AD therapy.

3. Conclusions

In this study, we developed a multifunctional hydrogel system via a typical Schiff base reaction and loaded it with a BP-MB nanocomposite. The fabricated BP-MB@Gel showed good thermo-sensitivity, injectability, and self-healing ability, which allowed it to undergo the sol–gel phase transition and prolonged its retention time in the nasal cavity. Accordingly, sustained drug release into the brain could be achieved for AD treatment. The synthetic BP-MB could cross the nasal mucosal barrier and could be internalized by neurons, exhibiting extraordinary ROS scavenging performance. It could protect cells from oxidative damage and ameliorate mitochondrial dysfunction. It also enabled the MB-mediated inhibition of cellular tau aggregation, eventually attenuating neuronal apoptosis. Subsequent in vivo experiments revealed that BP-MB@Gel significantly increased drug accumulation in the brain following IN administration, thereby largely moderating neuronal damage, regulating mitochondria function, and relieving p-tau accumulation and neuroinflammation in mouse models of tauopathy. Owing to these synergistic effects, the AD mouse models showed improved memory and cognitive abilities that were comparable to those of control mice. Hence, the proposed BP-MB@Gel served as a multi-pronged strategy for overcoming the challenges posed by the BBB and preventing the rapid loss of drugs from the nasal cavity. It also showed a broad application prospect in the management of AD and other neurodegenerative diseases.

Supporting Information

Supporting Information is available from the Wiley Online Library or from the author.

Acknowledgements

Y.L., Y.T., and G.C. contributed equally to this work. The authors gratefully acknowledge the support from the Guangdong Basic and Applied Basic Research Foundation (2019B1515120043) and the Key Fields of Biomedicine and Health Foundation of Colleges and Universities in Guangdong Province (2022ZDZX2017). All animal experimental procedures were carried out according to the protocol approved by the Animal Ethics Committee of Guangzhou University of Chinese Medicine (20220914009).

Conflict of Interest

The authors declare no conflict of interest.

Data Availability Statement

The data that support the findings of this study are available from the corresponding author upon reasonable request.

Keywords

Alzheimer's disease, black phosphorus, blood–brain barrier, intranasal hydrogel, methylene blue, tauopathy

Received: July 18, 2023
Revised: February 20, 2024
Published online: March 1, 2024

[1] J. Cummings, G. Lee, P. Nahed, M. Kambar, K. Zhong, J. Fonseca, K. Taghva, *Alzheimers Dementia* **2022**, *8*, e12295.
[2] M. A. Busche, B. T. Hyman, *Nat. Neurosci.* **2020**, *23*, 1183.
[3] B. J. Hanseeuw, R. A. Betensky, H. I. L. Jacobs, A. P. Schultz, J. Sepulcre, J. A. Becker, D. M. O. Cosio, M. Farrell, Y. T. Quiroz, E. C. Mormino, R. F. Buckley, K. V. Papp, R. A. Amariglio, I. Dewachter, A. Ivanoiu, W. Huijbers, T. Hedden, G. A. Marshall, J. P. Chhatwal, D. M. Rentz, R. A. Sperling, K. Johnson, *JAMA Neurol.* **2019**, *76*, 915.
[4] S. Wegmann, J. Biernat, E. Mandelkow, *Curr. Opin. Neurobiol.* **2021**, *69*, 131.
[5] C. Li, J. Götz, *Nat. Rev. Drug Discovery* **2017**, *16*, 863.
[6] a) J. Sinsky, K. Pichlerova, J. Hanes, *Int. J. Mol. Sci.* **2021**, *22*, 9207; b) Y. Soeda, A. Takashima, *Front. Mol. Neurosci.* **2020**, *13*, 590896.
[7] a) A. Chakravorty, C. T. Jetto, R. Manjithaya, *Front. Aging. Neurosci.* **2019**, *11*, 311; b) W. Wang, F. Zhao, X. Ma, G. Perry, X. Zhu, *Mol. Neurodegener.* **2020**, *15*, 30.
[8] Z. Liu, T. Li, P. Li, N. Wei, Z. Zhao, H. Liang, X. Ji, W. Chen, M. Xue, J. Wei, *Oxid. Med. Cell. Longevity* **2015**, *2015*, 352723.
[9] a) Q. Chen, Y. Du, K. Zhang, Z. Liang, J. Li, H. Yu, R. Ren, J. Feng, Z. Jin, F. Li, J. Sun, M. Zhou, Q. He, X. Sun, H. Zhang, M. Tian, D. Ling, *ACS Nano* **2018**, *12*, 1321; b) J. Zhao, F. Yin, L. Ji, C. Wang, C. Shi, X. Liu, H. Yang, X. Wang, L. Kong, *ACS Appl. Mater. Interfaces* **2020**, *12*, 44447.
[10] a) K. Hochgräfe, A. Sydow, D. Matenia, D. Cadinu, S. Könen, O. Petrova, M. Pickhardt, P. Goll, F. Morellini, E. Mandelkow, E. M. Mandelkow, *Acta Neuropathol. Commun.* **2015**, *3*, 25; b) W. Sun, S. Lee, X. Huang, S. Liu, M. Inayathullah, K. M. Kim, H. Tang, J. W. Ashford, J. Rajadas, *Sci. Rep.* **2016**, *6*, 34784; c) D. Tucker, Y. Lu, Q. Zhang, *Mol. Neurobiol.* **2018**, *55*, 5137.
[11] G. Zeng, Y. Chen, *Acta Biomater.* **2020**, *118*, 1.
[12] G. Qu, T. Xia, W. Zhou, X. Zhang, H. Zhang, L. Hu, J. Shi, X. F. Yu, G. Jiang, *Chem. Rev.* **2020**, *120*, 2288.

© 2024 Wiley-VCH GmbH

Downloaded for personal academic use. All rights reserved. https://papernode.online/

[13] a) G. Cheng, Z. Li, Y. Liu, R. Ma, X. Chen, W. Liu, Y. Song, Y. Zhang, G. Yu, Z. Wu, T. Chen, *J. Controlled Release* **2023**, *353*, 752; b) S. Xiong, Z. Li, Y. Liu, Q. Wang, J. Luo, X. Chen, Z. Xie, Y. Zhang, H. Zhang, T. Chen, *Biomaterials* **2020**, *260*, 120339.
[14] a) J. Hou, H. Wang, Z. Ge, T. Zuo, Q. Chen, X. Liu, S. Mou, C. Fan, Y. Xie, L. Wang, *Nano Lett.* **2020**, *20*, 1447; b) H. Lu, J. Wei, K. Liu, Z. Li, T. Xu, D. Yang, Q. Gao, H. Xiang, G. Li, Y. Chen, *ACS Nano* **2023**, *17*, 6131.
[15] M. D. Sweeney, Z. Zhao, A. Montagne, A. R. Nelson, B. V. Zlokovic, *Physiol. Rev.* **2019**, *99*, 21.
[16] C. P. Costa, J. N. Moreira, J. M. Sousa Lobo, A. C. Silva, *Acta Pharm. Sin. B* **2021**, *11*, 925.
[17] Q. S. Wang, K. Li, L. N. Gao, Y. Zhang, K. M. Lin, Y. L. Cui, *Biomater. Sci.* **2020**, *8*, 2853.
[18] E. Bellotti, A. L. Schilling, S. R. Little, P. Decuzzi, *J. Controlled Release* **2021**, *329*, 16.
[19] M. Agrawal, S. Saraf, S. Saraf, S. K. Dubey, A. Puri, U. Gupta, P. Kesharwani, V. Ravichandiran, P. Kumar, V. G. M. Naidu, U. S. Murty, Ajazuddin, A. A., *J. Controlled Release* **2020**, *327*, 235.
[20] S. Correa, A. K. Grosskopf, H. L. Hernandez, D. Chan, A. C. Yu, L. M. Stapleton, E. A. Appel, *Chem. Rev.* **2021**, *121*, 11385.
[21] M. L. Formica, D. A. Real, M. L. Picchio, E. Catlin, R. F. Donnelly, A. J. Paredes, *Appl. Mater. Today.* **2022**, *29*, 101631.
[22] A. Jayakumar, V. K. Jose, J.-M. Lee, *Small Methods* **2020**, *4*, 1900735.
[23] Z. Li, F. Zhou, Z. Li, S. Lin, L. Chen, L. Liu, Y. Chen, *ACS Appl. Mater. Interfaces* **2018**, *10*, 25194.
[24] a) L. Jin, P. Hu, Y. Wang, L. Wu, K. Qin, H. Cheng, S. Wang, B. Pan, H. Xin, W. Zhang, X. Wang, *Adv. Mater.* **2020**, *32*, 1906050; b) W. Chen, J. Ouyang, H. Liu, M. Chen, K. Zeng, J. Sheng, Z. Liu, Y. Han, L. Wang, J. Li, L. Deng, Y. N. Liu, S. Guo, *Adv. Mater.* **2017**, *29*, 1603864.
[25] a) Q. Zhao, W. Ma, B. Pan, Q. Zhang, X. Zhang, S. Zhang, B. Xing, *Environ. Sci. Nano* **2018**, *5*, 1454; b) J. Wang, Z. Zhang, D. He, H. Yang, D. Jin, J. Qu, Y. Zhang, *Sustainability* **2020**, *12*, 8335.
[26] R. Bai, J. Guo, X.-Y. Ye, Y. Xie, T. Xie, *Ageing Res. Rev.* **2022**, *77*, 101619.
[27] X. Mu, J. Wang, Y. Li, F. Xu, W. Long, L. Ouyang, H. Liu, Y. Jing, J. Wang, H. Dai, Q. Liu, Y. Sun, C. Liu, X. D. Zhang, *ACS Nano* **2019**, *13*, 1870.
[28] B. Hu, M. Gao, K. O. Boakye-Yiadom, W. Ho, W. Yu, X. Xu, X. Q. Zhang, *Bioact. Mater.* **2021**, *6*, 4592.
[29] a) S. Pund, G. Rasve, G. Borade, *Eur. J. Pharm. Sci.* **2013**, *48*, 195; b) R. J. Majithiya, P. K. Ghosh, M. L. Umrethia, R. S. Murthy, *AAPS PharmSciTech* **2006**, *7*, E80.
[30] B. He, P. Lin, Z. Jia, W. Du, W. Qu, L. Yuan, W. Dai, H. Zhang, X. Wang, J. Wang, X. Zhang, Q. Zhang, *Biomaterials* **2013**, *34*, 6082.
[31] Y. Yin, H. Deng, K. Wu, B. He, W. Dai, H. Zhang, J. Fu, Y. Le, X. Wang, Q. Zhang, *J. Controlled Release* **2020**, *323*, 600.
[32] A. B. Dyve Lingelem, J. Bergan, K. Sandvig, *Traffic* **2012**, *13*, 443.
[33] a) L. M. de Medeiros, M. A. De Bastiani, E. P. Rico, P. Schonhofen, B. Pfaffenseller, B. Wollenhaupt-Aguiar, L. Grun, F. Barbé-Tuana, E. R. Zimmer, M. A. A. Castro, R. B. Parsons, F. Klamt, *Mol. Neurobiol.* **2019**, *56*, 7355; b) P. K. Kamat, S. Rai, S. Swarnkar, R. Shukla, C. Nath, *Mol. Neurobiol.* **2014**, *50*, 852.
[34] M. Oz, D. E. Lorke, M. Hasan, G. A. Petroianu, *Med. Res. Rev.* **2011**, *31*, 93.
[35] Y. Esmaeili, Z. Yarjanli, F. Pakniya, E. Bidram, M. J. Łos, M. Eshraghi, D. J. Klionsky, S. Ghavami, A. Zarrabi, *J. Controlled Release* **2022**, *345*, 147.
[36] F. Xu, Y. Wu, Q. Yang, Y. Cheng, J. Xu, Y. Zhang, H. Dai, B. Wang, Q. Ma, Y. Chen, F. Lin, C. Wang, *Adv. Mater.* **2022**, *34*, 2207107.
[37] S. Bhatia, R. Rawal, P. Sharma, T. Singh, M. Singh, V. Singh, *Curr. Neuropharmacol.* **2022**, *20*, 675.
[38] a) Y. Zhang, J. Fang, S. Ye, Y. Zhao, A. Wang, Q. Mao, C. Cui, Y. Feng, J. Li, S. Li, M. Zhang, H. Shi, *Nat. Commun.* **2022**, *13*, 1685; b) Y. Liu, H. Hong, J. Xue, J. Luo, Q. Liu, X. Chen, Y. Pan, J. Zhou, Z. Liu, T. Chen, *ACS Appl. Mater. Interfaces* **2021**, *13*, 37746.
[39] X. Luo, X. Gong, L. Su, H. Lin, Z. Yang, X. Yan, J. Gao, *Angew. Chem., Int. Ed. Engl.* **2021**, *60*, 1403.
[40] L. Feng, C. Dou, Y. Xia, B. Li, M. Zhao, P. Yu, Y. Zheng, A. M. El-Toni, N. F. Atta, A. Galal, Y. Cheng, X. Cai, Y. Wang, F. Zhang, *ACS Nano* **2021**, *15*, 2263.
[41] P. Rawat, U. Sehar, J. Bisht, A. Selman, J. Culberson, P. H. Reddy, *Int. J. Mol. Sci.* **2022**, *23*, 12841.
[42] K. R. Brunden, C. Ballatore, A. Crowe, A. B. Smith, 3rd, V. M. Lee, J. Q. Trojanowski, *Exp. Neurol.* **2010**, *223*, 304.
[43] a) L. R. Bevilaqua, J. I. Rossato, J. S. Bonini, J. C. Myskiw, J. R. Clarke, S. Monteiro, R. H. Lima, J. H. Medina, M. Cammarota, I. Izquierdo, *Neural Plast.* **2008**, *2008*, 595282; b) U. A. Khan, L. Liu, F. A. Provenzano, D. E. Berman, C. P. Profaci, R. Sloan, R. Mayeux, K. E. Duff, S. A. Small, *Nat. Neurosci.* **2014**, *17*, 304.
[44] A. von Gunten, E. Kövari, T. Bussière, C. B. Rivara, G. Gold, C. Bouras, P. R. Hof, P. Giannakopoulos, *Neurobiol. Aging* **2006**, *27*, 270.
[45] J. T. Wang, A. C. Rodrigo, A. K. Patterson, K. Hawkins, M. M. S. Aly, J. Sun, K. T. Al Jamal, D. K. Smith, *Adv. Sci.* **2021**, *8*, e2101058.
[46] M. J. Majcher, A. Babar, A. Lofts, A. Leung, X. Li, F. Abu-Hijleh, N. M. B. Smeets, R. K. Mishra, T. Hoare, *J. Controlled Release* **2021**, *330*, 738.
[47] S. Calafate, A. Buist, K. Miskiewicz, V. Vijayan, G. Daneels, B. de Strooper, J. de Wit, P. Verstreken, D. Moechars, *Cell Rep.* **2015**, *11*, 1176.
[48] S. Baker, J. Götz, *Acta Neuropathol. Commun.* **2016**, *4*, 32.
[49] a) D. O. Seo, D. O'Donnell, N. Jain, J. D. Ulrich, J. Herz, Y. Li, M. Lemieux, J. Cheng, H. Hu, J. R. Serrano, X. Bao, E. Franke, M. Karlsson, M. Meier, S. Deng, C. Desai, H. Dodiya, J. Lelwala-Guruge, S. A. Handley, J. Kipnis, S. S. Sisodia, J. I. Gordon, D. M. Holtzman, *Science* **2023**, *379*, eadd1236; b) P. Jirkof, *J. Neurosci. Methods* **2014**, *234*, 139.
[50] C. Fischer, H. Endle, L. Schumann, A. Wilken-Schmitz, J. Kaiser, S. Gerber, C. F. Vogelaar, M. H. H. Schmidt, R. Nitsch, I. Snodgrass, D. Thomas, J. Vogt, I. Tegeder, *Cell. Mol. Life Sci.* **2021**, *78*, 1029.
[51] X. Li, W. Chen, K. Pan, H. Li, P. Pang, Y. Guo, S. Shu, Y. Cai, L. Pei, D. Liu, H. K. Afewerky, Q. Tian, L. Q. Zhu, Y. Lu, *Nat. Neurosci.* **2018**, *21*, 1239.
[52] A. R. Abela, A. Rahbarnia, S. Wood, A. D. Lê, P. J. Fletcher, *Psychopharmacology* **2019**, *236*, 1875.
[53] J. Nithianantharajah, A. G. McKechanie, T. J. Stewart, M. Johnstone, D. H. Blackwood, D. St Clair, S. G. Grant, T. J. Bussey, L. M. Saksida, *Sci. Rep.* **2015**, *5*, 14613.
[54] a) H. Li, C. Guglielmetti, Y. J. Sei, M. Zilberter, L. M. Le Page, L. Shields, J. Yang, K. Nguyen, B. Tiret, X. Gao, N. Bennett, I. Lo, T. L. Dayton, M. Kampmann, Y. Huang, J. C. Rathmell, M. V. Heiden, M. M. Chaumeil, K. Nakamura, *Cell Rep.* **2023**, *42*, 112335; b) X. Y. Li, W. W. Men, H. Zhu, J. F. Lei, F. X. Zuo, Z. J. Wang, Z. H. Zhu, X. J. Bao, R. Z. Wang, *Int. J. Mol. Sci.* **2016**, *17*, 1707.
[55] P. K. Kamat, S. Tota, R. Shukla, S. Ali, A. K. Najmi, C. Nath, *Pharmacol. Biochem. Behav.* **2011**, *100*, 311.
[56] W. Zhang, H. Chen, L. Ding, J. Gong, M. Zhang, W. Guo, P. Xu, S. Li, Y. Zhang, *Adv. Sci.* **2021**, *8*, 2004555.
[57] J. Song, X. Yang, M. Zhang, C. Wang, L. Chen, *J. Alzheimers Dis.* **2021**, *84*, 557.
[58] S. Baker, J. Götz, *Acta Neuropathol. Commun.* **2016**, *4*, 32.

© 2024 Wiley-VCH GmbH

Downloaded for personal academic use. All rights reserved. https://papernode.online/